PHYSICS OF REACTOR SAFETY

Quarterly Report

April—June 1979

RGONNE NATIONAL LABORATORY, ARGONNE, ILLINOIS

repared for the U. S. NUCLEAR REGULATORY COMMISSION
nder Interagency Agreement DOE 40-550-75

Available from
National Technical Information Service
Springfield, Virginia 22161

NUREG/CR-1096
ANL-79-76

ARGONNE NATIONAL LABORATORY
9700 South Cass Avenue
Argonne, Illinois 60439

PHYSICS OF REACTOR SAFETY

Quarterly Report
April—June 1979

Applied Physics Division

August 1979

Previous reports in this series

ANL-78-85	April—June 1978
ANL-78-106	July—September 1978
ANL-79-19	October—December 1978
ANL-79-37	January—March 1979

Prepared for the Division of Reactor Safety Research
Office of Nuclear Regulatory Research
U. S. Nuclear Regulatory Commission
Washington, D. C. 20555
Under Interagency Agreement DOE 40-550-75

NRC FIN Nos. A2015, A2018, A2045

TABLE OF CONTENTS

Page

III. THREE-DIMENSIONAL CODE DEVELOPMENT FOR CORE THERMAL HYDRAULIC ANALYSIS OF LMFBR ACCIDENTS UNDER NATURAL CONVECTION CONDITIONS

LIST OF FIGURES

LIST OF FIGURES (CONTD)

LIST OF FIGURES (CONTD)

LIST OF TABLES

PHYSICS OF REACTOR SAFETY

Quarterly Report
April-June 1979

ABSTRACT

This Quarterly progress report summarizes work done during the months of April-June 1979 in Argonne National Laboratory's Applied Physics and Components Technology Divisions for the Division of Reactor Safety Research of the U. S. Nuclear Regulatory Commission. The work in the Applied Physics Division includes reports on reactor-safety research and technical coordination of the RSR safety analysis program by members of the Reactor Safety Appraisals Group, Monte Carlo analysis of safety-related critical assembly experiments by members of the Reactor Computations Group, and planning of safety-related critical experiments by members of the Zero Power Reactor (ZPR) Planning and Experiments Group. Work on reactor core thermal-hydraulics was performed in ANL's Components Technology Division.

I. REACTOR SAFETY MODELING AND ASSESSMENT

(A2015)

A. Summary

Studies with the FPIN code indicate the possibility of cladding failure due to differential expansion of solid fuel and cladding during certain LOF-TOP transients. Since the failure will typically occur at a lower fuel melt fraction, molten fuel ejection will probably not occur immediately, so that the safety significance of failure of this type depends on subsequent events such as additional cladding failures in the pin.

The data available for failure strain of irradiated 20% cold-worked Type 316 stainless steel cladding under transient heating has been reviewed as part of an effort to separate modeling deficiencies from uncertainties in the cladding properties. The variation of diametral strain at failure as a function of temperature at failure is masked by the effect of neutron fluence in the data surveyed. The variation of diametral strain at failure as a function of fast neutron fluence is scattered; however, the maximum diametral strain bounding the scatter decreases with increasing fluence.

Development of BIFLO has reached the status of being able to perform steady-state initialization and proceed into transient boiling and voiding using a homogeneous model. The results up to boiling initiation are in excellent agreement with SAS3D. The experimental data base and calculational models available for BIFLO verification are being reviewed, and several existing subchannel codes are being made operational at ANL. A survey of experiment data relating to incipient boiling superheat in sodium has been conducted; inert gas and oxide concentrations in the system are found to be important effects but insufficient data is available for predicting superheat under generalized reactor conditions.

A compressible treatment of sodium in the channel has been implemented into a version of EPIC for use in analyzing pressure propagation in autoclave geometry. The distributed particle-in-cell treatment for channel fuel has been incorporated into FRAM-0 (SAS3D/FRESS/EPIC).

Calculations have been completed with FRAM-0 for the USNRC contribution to the WAC study for a 1$/s TOP in a BOL core. The treatments of post pin-failure fuel motion and disassembly in FRAM-0 differ significantly from the treatments in codes used by the European participants, and this complicates comparison of results. The initial calculations (to 100 ms past fuel-pin failure) with FRAM-0 have been completed for a 10¢/s TOP in an irradiated core for the WAC study.

B. Fuel Pin Failure Studies

1. FPIN Calculations for LOF-TOP Conditions (H. H. Hummel)

The FPIN code[1] has been used to calculate LMFBR fuel failure from differential expansion of solid fuel and clad during a LOF-TOP event with

conditions obtained from a SAS calculation. The geometry in these calculations was the same as that for the TOP calculations reported in our January-March, 1979, Quarterly Report,[2] except that four axial nodes were used, with the first node extending from 54.4 to 62.2 cm of the 101 cm core height, and the other three nodes as before, that is, from 62.2-77.8, 77.8-93.3, and 93.3-101.1 cm. (Note that there is a slight correction to the previously given axial dimensions.) Coolant temperature rise was accounted for in these calculations by specifying the outer clad temperature for each node as a function of time, obtained from a SAS calculation, instead of the coolant temperature into the first node as was previously the case. Transient power and clad temperatures are given in Table I, with pin failure results given in Table II.

TABLE I. Transient Power and Clad Temperatures

Time, s	Normalized Power	Outer Clad Temperature, °K			
		Axial Node			
		1	2	3	4
0.0	1.00	752	772	793	808
12.0	1.00	858	899	944	970
24.0	1.00	949	1009	1075	1114
25.8	1.31				
26.00	3.33				
26.15	6.73				
26.18	9.13				
26.21	14.0				
26.260	29.9	1130	1186	1236	1255
26.280	39.7	1193	1247	1288	1296
26.298	56.2				
26.317	83.1	1257	1304	1336	1333
26.326	143				
26.328	180	1304	1346	1365	1354
26.330	221	1316	1358	1373	1368

A variable gap conductance was used in these calculations, using the Chow model as before,[2] with higher and lower gap conductance again specified by varying the assumed bond gas composition. The assumed steady-state gap for each axial node was again based on cold-to-hot gap calculations. The range of gap sizes indicated in Table II is within the range that might reasonably be expected at operating conditions. The axial variation of gap size is based on assuming a uniform cold gap. In practice the gap at operating conditions might be closed over much of the pin, which would lessen the tendency indicated here for failure from solid fuel expansion to occur only near the core midplane. In most of the cases in Table II the calculation was carried out for only the first two axial nodes, because with the assumed initial gap sizes failure would not occur in the other nodes.

As discussed previously[2] interest is focused on events occurring below 0.50 melt fraction, as at higher melt fractions solid fuel mechanical strength becomes small and other mechanisms not properly accounted for in the

TABLE II. FPIN Results for LOF-TOP Cases

Prob.	Case	Axial Node	Initial Gap, cm	Initial Crack Radius, cm	Gas Composition, %			Initial Gap Cond, Watts/cm^2-°K	Gap Conductance at Failure Watts/cm^2-°K	Max.[a] Life Fr.	Failure Time, s	Fuel Melt Fr. at Failure	Clad Failure Temp, °K	Peak Clad Stress, bars	Failure Clad Stress, bars
					He	Xe	Kr								
117	1	1	0.0006	0.12	25	65	10	0.48	1.62	1.00	26.260	0.22	1168	2228	2217
		2	0.0009					0.42	1.21	0.00				622	
		3	0.0015					0.33	1.24	0.00					
		4	0.0025					0.25	0.55	0.00					
118	2	1	0.0006	0.25	25	65	10	0.48	1.62	1.00	26.265	0.25	1171	2215	2194
		2	0.0009					0.42	1.59	0.33				1689	
		3	0.0015					0.33	1.33	0.00				1221	
		4	0.0025					0.25	0.56	0.00					
132	3	1	0.0007	0.12	25	65	10	0.46		0.00				1088	
		2	0.0010					0.40		0.00				919	
135	4	1	0.0007	0.25	25	65	10	0.46	1.65	1.00	26.279	0.40	1206	2162	1779
		2	0.0010					0.40	1.65	0.25				1655	
138	5	1	0.0010	0.12	50	43	7	0.79	3.02	1.00	26.250	0.08	1166	2330	2330
		2	0.0013					0.70	2.28	0.00				1108	
137	6	1	0.0010	0.25	50	43	7	0.79	3.04	1.00	26.255	0.10	1168	2316	2326
		2	0.0013					0.70	2.93	0.59				1759	
142	7	1	0.0015	0.12	50	43	7	0.65		0.00				750	
		2	0.0018					0.59		0.00				842	
141	8	1	0.0015	0.25	50	43	7	0.65		0.76				2109	
		2	0.0018					0.59		0.12				1599	

[a]Up to ~0.50 melt fraction.

present calculations become dominant for fuel failure. Fission gas was assumed released on fuel melting, but was not a significant factor in the present calculations below 0.50 melt fraction. Fuel cracking and stress relaxation were taken into account in all the present calculations. The effect of suppressing axial cracking was found to be negligible.

For all the calculations in Table II the Larson-Miller parameter correlation used in the FPIN life fraction calculations was that for clad fluence between 2 and 3 × 10^{22} n/cm^2, reported by Johnson et al.[3] Use of a correlation for fluence between 0 and 1 × 10^{22} resulted in no failures occurring.

Note that in Table II results are given for an assumed initial crack radius of 0.12 cm (for all nodes) and also 0.25 cm. Some sensitivity of FPIN results to the assumed radius is apparent. In the FPIN modeling of cracking, cracks close when the stress becomes compressive, but do not heal, and can open again when the compressive stress is relieved. It was found that there was a tendency for cracks to reopen suddenly and relieve clad loading with a net inward movement of fuel, which especially occurred when the melt front reached the original crack boundary. This did not occur if the fuel was not initially cracked. The difference in assumed initial crack radius appeared in the present study to be equivalent to ~0.0003 cm in initial gap size in affecting clad failure. The fact that fuel cracking leads to less clad loading rather than more seems somewhat anomalous, because cracking eliminates fuel tensile strength in the outer part of the pin, which restrains fuel expansion. This is outweighed in the present case by inward motion of the cracked fuel, possible because of the presence of a central void.

FPIN does not model crack volume, which has been found important in other studies.[4] The developers of FPIN plan to make this improvement, which may affect the cracked fuel behavior noted here.

As found previously, an increased gap conductance tends to increase clad failure by solid fuel expansion because of the associated decrease in fuel stress relaxation and melting. Note that the fuel melt fraction at failure depends strongly on the assumed gap conductance. The initial gap sizes at which clad failure starts to occur from solid fuel expansion in the present LOF-TOP studies are summarized as a function of gap conductance and initial crack radius in Table III. Failure would of course occur earlier and at smaller fuel melt fractions for smaller gaps than those indicated.

In summary, clad failure from solid fuel expansion seems to be a possibility for the type of LOF-TOP transient indicated here. Since failure will typically occur at a low melt fraction, molten fuel ejection will probably not occur immediately, so that the safety significance of failure of this type depends on subsequent events such as additional clad failures elsewhere in the pin.

In the TOP cases calculated with FPIN reported previously,[2] an initial crack radius of 0.25 cm was assumed. A recheck of these cases using a radius of 0.12 cm did not show significant differences except in Case 2 in Table III of the previous report, in which failure no longer occurred in axial node 3 when the smaller initial crack radius was assumed because of the reopening of cracks referred to above.

TABLE III. Failure Threshold Radial Gap in cm. for LOF-TOP

	Initial Crack Radius, cm	
Initial Gap Conductance	0.12	0.25
Lower	0.0006 - 0.0007	0.0007 - 0.0010
Higher	0.0010 - 0.0015	0.0010 - 0.0015

2. Failure Strain of Irradiated 20% Cold-Worked Type 316 Stainless Steel Cladding During Transient Heating (Kalimullah)

a. Introduction: In order to calculate failure conditions in an overpower transient for irradiated LMFBR fuel pin cladding it is necessary to be able to characterize the strength and strain of the cladding as a function of failure temperature, heating rate, fast fluence and other important variables. It is important to be able to state error limits for such characterization in order that discrepancies between calculated and experimental failure conditions resulting from model deficiencies rather than from uncertainties in cladding properties can be identified. A review of burst rupture strength of 20% cold-worked type 316 stainless steel cladding during transient heating is given in Reference 5, and the status of the diametral inelastic strain to failure (defined as $(D-D_o)/D_o$ where D_o and D are the initial and post-failure diameters of the cladding) is discussed here. In the calculation of fission gas pressure in a segment of the fueled portion of the pin, the importance of the cladding diametral strain arises from its contribution to the volume available to the fission gas. In the calculation of fuel-cladding solid-to-solid contact pressure, the cladding diametral inelastic strain can significantly relax the pressure. If the maximum strain criterion is chosen for cladding failure calculation, then the diametral failure strain and its error limits are key parameters.

b. Selection of Data Base: Table IV contains all the published HEDL Fuel Cladding Transient Tester (FCTT) burst test results for 20% cold-worked type 316 stainless steel cladding specimens taken from the fueled region of mixed-oxide pins irradiated in EBR-II (fast fluence, E > 0.1 MeV, in the range $0.66 - 5.82 \times 10^{22}$ neutron/cm^2) and tested at 200°F/sec heating rate (60 tests).[6,7] Seven variables are believed to influence the diametral failure strain: 1) failure temperature, 2) fast neutron fluence, 3) heating rate, 4) circumferential temperature variation, 5) axial temperature variation, 6) specimen taken from fueled or unfueled region of pin and 7) irradiation temperature. The variations of diametral failure strain with failure temperature and fast neutron fluence are reviewed here. The choice of values of the other five variables, i.e., variables (3) to (7), for use in calculating failure conditions in an overpower transient is first discussed:

TABLE IV. FCTT Burst Test Results for Irradiated Cladding Taken from the Fueled Region at 200°F/s Heating Rate[a]

Serial No.	Pin	Distance above fuel bottom, inch	Midwall irradiation temp., °F	Average fluence, 10^{22} n/cm^2	Gas pressure, ksi	Irradiated failure temp., °F	Diametral failure Strain, %	Failure stress, ksi
1	P-23A-21	7.4- 9.9	1105	3.94	4.0	1790	0.41	28.8
2		10.3-12.8	1186	3.28	4.0	1770	0.52	28.8
3	P-23A-31	0.8- 3.3	830	1.61	6.0	1610	0.35	43.2
4		3.6- 6.1	956	1.92	4.0	1800	0.70	28.8
5	P-23A-32	0.8- 3.3	827	1.61	14.3	1125	0.13[b]	103.0
6	P-23A-59C	0.8- 3.3	827	0.79	4.0	1805	1.13	28.8
7		7.3- 9.8	1106	0.89	6.0	1585	0.35	43.2
8	P-23A-60D	3.6- 6.1	954	1.04	10.0	1420	0.61	72.0
9	N-E-029	1.0- 3.5	820	1.49	13.5	1115	-	97.2
10	N-E-049	4.0- 6.5	909	1.69	13.5	1020	0.52	97.2
11		9.3-11.8	1060	1.48	10.0	1185	0.56	72.0
12		11.8-14.3	1060	1.13	4.0	1600	0.15[c]	28.8
13	PNL-9-13	3.5- 6.0	820	5.15	4.0	1380	0.04	28.8
14		9.5-12.0	940	4.51	4.0	1546[d]	0.10	28.8
15	PNL-9-30	0.6- 3.1	762	4.55	6.0	1414	0.07	43.2
16	PNL-9-60	1.0- 3.5	762	5.06	14.3	1156	0.22	103.0
17		7.0- 9.5	863	5.82	2.5	1665	0.10	18.0
18		12.0-14.5	920	3.93	10.0	1100	0.28	72.0
19	PNL-11-48A	10.8-13.3	980	3.59	6.0	1545	0.10	43.2
20	PNL-23B-2A	4.0- 6.5	981	4.69	10.0	1230	0.28	72.0
21	PNL-23B-14A	1.2- 3.6	830	4.01	13.365	1096	0.17	96.2
22		3.6- 6.1	937	4.58	13.250	762	>1.0	95.4
23		8.2-10.7	1129	4.41	6.0	1588	1.02	43.2
24		11.2-13.6	1235	3.43	6.0	1650	0.70	43.2
25	PNL-23B-35B	4.0- 6.5	964	4.69	2.5	1794	0.25	18.0
26		7.3- 9.8	1106	4.62	4.0	1784	0.21	28.8
27		10.5-13.0	1230	3.75	4.0	1808	0.83	28.8
28	P23C-3A	(-1.0)- 1.5	743	0.70	13.5	1170	0.23	97.2
29		1.5- 4.0	822	0.93	10.0	1354	0.75	72.0
30		4.0- 6.5	895	1.04	10.0	1195	0.17	72.0
31		7.0- 9.5	982	1.03	10.0	1384	0.99	72.0
32	P23C-49C	4.0- 6.5	896	1.04	6.0	1592	0.30	43.2

[a]Compiled from References 6 and 7.

[b]Extensive tear failure, strain may be erroneously low.

[c]Specimen failed at wear mark (depth = 1.5 mils).

[d]Specimen did not fail at the wear mark.

TABLE IV. (Contd)

Serial No.	Pin	Distance above fuel bottom, inch	Midwall irradiation temp., °F	Average fluence, 10^{22} n/cm^2	Gas pressure, ksi	Irradiated failure temp., °F	Diametral failure Strain, %	Failure stress, ksi
35	P23C-71G	4.1- 6.6	930	1.03	9.0	1430	0.40	64.8
36		7.6-10.1	1053	1.00	8.0	1480	0.91	57.6
37		10.1-12.6	1083	0.85	5.0	1732	0.26	36.0
38	P23C-25B	(-1.0)- 1.5	743	0.70	13.5	1182	0.33	97.2
39		1.5- 4.0	821	0.92	10.0	1380	0.58	72.0
40		4.0- 6.5	886	1.03	10.0	1370	0.75	72.0
41		6.5- 9.0	958	1.03	10.0	1422	1.14	72.0
42		9.0-11.5	1032	0.93	4.0	1853	1.3	28.8
43		12.0-14.5	1072	0.66	4.0	1892	1.87	28.8
44	P23C-29B	1.1- 3.6	812	0.88	6.0	1406	1.34	43.2
45		3.6- 6.1	884	1.01	6.0	1710	1.26	43.2
46		6.1- 8.6	952	1.04	6.0	1695	0.94	43.2
47		8.6-11.1	1020	0.96	6.0	1606	1.24	43.2
48		12.1-14.6	1073	0.67	6.0	1682	0.93	43.2
49	NUMEC F-N-005	7.5- 9.5	890	3.05	2.5	1940	0.8	18.0
50		2.0- 4.5	800	2.90	4.0	1670	0.4	28.8
51	NUMEC F-N-035	7.0- 9.5	935	3.05	4.0	1525	0.25	28.8
52	NUMEC F-N-159	(-0.5)-2.0	743	2.15	6.0	1520	0.3	43.2
53	NUMEC F-N-070	0.5- 3.2	781	2.40	10.0	1210	0.2	72.0
54	NUMEC F-N-027	4.5- 7.0	870	3.05	10.0	1310	0.4	72.0
55		12.0-14.5	983	1.95	10.0	1205	0.7	72.0
56	NUMEC F-N-070	12.0-14.5	995	1.90	10.0	1070	0.29	72.0
57	NUMEC F-N-027	(-0.5)-2.0	743	2.25	13.5	1120	0.4	97.2
58	PNL-10-23	1.5- 4.0	798	3.50	4.0	1770	0.65	28.8
59		8.5-11.0	953	3.65	4.0	1400	0.20	28.8
60	PNL-11-12	7.5-10.0	888	2.35	10.0	1230	0.17	72.0

Heating rate: Since heating rates of 200°F/sec or even considerably larger are typical of LMFBR transient overpower (TOP) accidents, and extrapolations of failure strain for higher heating rates from the two values of failure strain at 10°F/sec and 200°F/sec heating rates used in FCTT test[6,7] may be misleading, it seems appropriate at present to use the 200°F/sec data for all LMFBR TOP analyses no matter what heating rates are encountered. Accordingly, only the 200°F/sec data are included in Table IV.

Circumferential temperature variation: Circumferentially averaged temperature being the same, zircaloy cladding with circumferential temperature variation has been found to fail with a lower diametral strain than otherwise similar cladding with uniform temperature, and qualitatively a similar behavior is expected for stainless steel cladding also.[8] Although there is some circumferential variation of cladding temperature in an actual LMFBR, there was no such variation in the FCTT tests, and its effect on failure strain cannot be evaluated at present.

Axial temperature variation: The cladding temperature was maintained uniform over ~1.5 inch of the ~2.5 inch length of the specimens. A portion of the uniform temperature length at each end is affected by the steep temperature gradient present during the test and the diametral strain varies along these two portions of the uniform temperature length. If the specimen happens to fail with a pinhole, then a uniform temperature length of ~1.5 inch has been determined to have a middle portion with almost constant diametral strain.[9] (Actually, in Ref. 9, this has been determined for unirradiated 20% cold-worked type 316 stainless steel cladding. Since the failure strain of irradiated cladding is smaller than that of unirradiated cladding under similar conditions, the irradiated cladding is expected to have a comparatively larger middle portion with almost constant diametral strain.) It is reasonable to take this constant diametral strain as the diametral failure strain.

The type of failure (pinhole or burst rupture) of the tests 1 to 48 in Table IV is reported in Ref. 6, and excluding the five tests 13, 14, 17, 19 and 48 the failure is of the burst rupture type in the other 43 cases. The length and width of the breach tend to increase with increasing gas pressure; the length varies from 0.2 to 0.5 inch and the width ranges up to 0.25 inch.[6] A portion of the specimen length at each end of the breach length is strongly affected by the rupture, and the diametral strain varies along these portions of the specimen length. The diametral failure strain could not be measured either over these portions of the specimen length or over a portion at each end of the uniform temperature zone which is affected by the steep temperature gradient, but could be measured over some remaining portion with almost constant diametral strain. In the case of burst rupture failure, ~2.5 inch long specimens of unirradiated 20% cold-worked type 316 stainless steel cladding have been found to have no portion of almost constant diametral strain,[9] but such a portion could still be found in the irradiated cladding since the failure strain of irradiated cladding is smaller than that of unirradiated cladding under similar conditions. It is not certain at present that ~1.5 inch long uniform temperature zone of ~2.5 inch long irradiated cladding specimen will have a portion with almost constant diametral strain in the case of burst rupture failure, and the diametral failure strain measured in the FCTT tests[6,7] (contained in Table IV here) is sometines based on subjective judgement and its effect is included in uncertainties in the present review. In the absence of anything better, a rough estimate of this uncertainty may be obtained by noting that the diametral failure strain measured for unirradiated cladding at 10°F/sec heating rate using 6 inch or longer specimens[9] is about 3 times larger than that measured in the FCTT tests[10] using ~2.5 inch long specimens. If the same ratio is assumed for irradiated cladding at 200°F/sec heating rate, the diametral failure strains in Table IV should be increased by a factor of about three.

Specimen taken from fueled or unfueled region of pin: Cladding specimens taken from the fueled region of pins show lower strength, lower failure temperature and lower diametral failure strain than specimens taken from above or below the fuel column. Besides irradiation damage, chemical attack of mixed oxide fuel and fission products on the cladding inside surface and helium embrittlement (due to helium produced by (n,α) reactions in the stainless steel and by ternary fissions) are expected to be responsible for the greater degradation of fuel-column-region specimens.[6] The presence of a helium concentration gradient up to ~3 mils into the cladding thickness from

the inner surface (due to penetration and deposition of ternary fission-produced helium) could possibly produce a severe degradation of cladding mechanical properties.

Two types of chemical attack of fuel and fission products have been observed: a) matrix attack which causes a uniform transgranular corrosion with loss of cladding wall thickness from a region of the inner surface, and b) intergranular attack which causes corrosion along the grain boundaries loosening the grains of the cladding material, and is generally nonuniform in depth and sporadic in occurrence.[11] The latter is the predominant type of inner surface corrosion and is supposed to be a key reason for degrading fuel column cladding specimens. The variation of the maximum depth of attack with the fuel O/M ratio, burnup, cladding inner surface temperature, etc. have been reviewed and is found to be uncertain from 0 to more than 80 μm for burnups greater than about 35000 MWd/T.[12] The quantitative prediction of fuel-attack is not currently possible. In the present discussion of diametral failure strain, the fuel adjacency effect is included in uncertainties. In Table IV, cladding specimens taken only from the fueled region of pins have been included because in an actual LMFBR transient overpower accident the pin is expected to fail somewhere in the fueled region. In this way the appropriate effects of fuel-attack are accounted for.

The sporadic nature of the fuel adjacency effect is clearly exhibited by a comparison of the diametral failure strains of the specimens 29, 30 and 31 (see Table IV) taken from the same pin (P23C-3A) and tested at the same gas pressure (10 ksi). The specimens 39, 40 and 41 taken from the pin P23C-25B and tested at the same gas pressure (10 ksi) also show the sporadic nature of the fuel adjacency effect.

Irradiation temperature: The time averaged midwall irradiation temperature in Table IV varies in the range 743-1235°F. The presence of mixed oxide fuel and neutron fluence produces a much larger change in cladding mechanical properties than does the variation in irradiation temperature below 1100°F.[6,7] Irradiation temperatures above 1100°F seem to produce a smaller degradation of mechanical properties than do irradiation temperatures below 1100°F, but the evidence is quite weak[6] because there are only 7 tests (see Table IV) with irradiation temperature above 1100°F (4 tests at a gas pressure of 4 ksi and 3 tests at 6 ksi). In any case, the effect of irradiation temperature variation is masked by the effects of neutron fluence and fuel-attack, and therefore it is included in uncertainties in the present discussion of diametral failure strain.

c. Analysis of the Data: The unirradiated cladding shows a maximum diametral failure strain at a failure temperature of ~2000°F during transient heating.[10] To determine whether a similar variation existed for the irradiated cladding or not, all the diametral failure strains in Table IV (excluding the tests 5, 9 and 22 for which the diametral failure strain is unknown or doubtful) have been plotted against failure temperature in Fig. 1. The data have been grouped based on fast neutron fluence: 1) fluence range $2.15\text{-}5.82 \times 10^{22}$ neutrons/cm^2, and 2) fluence range $0.66 - 1.95 \times 10^{22}$ neutrons/cm^2. Neither group of data shows a variation of diametral failure strain with failure temperature similar to that shown by the unirradiated cladding. It seems that the diametral failure strains for the higher fluence group of specimens are

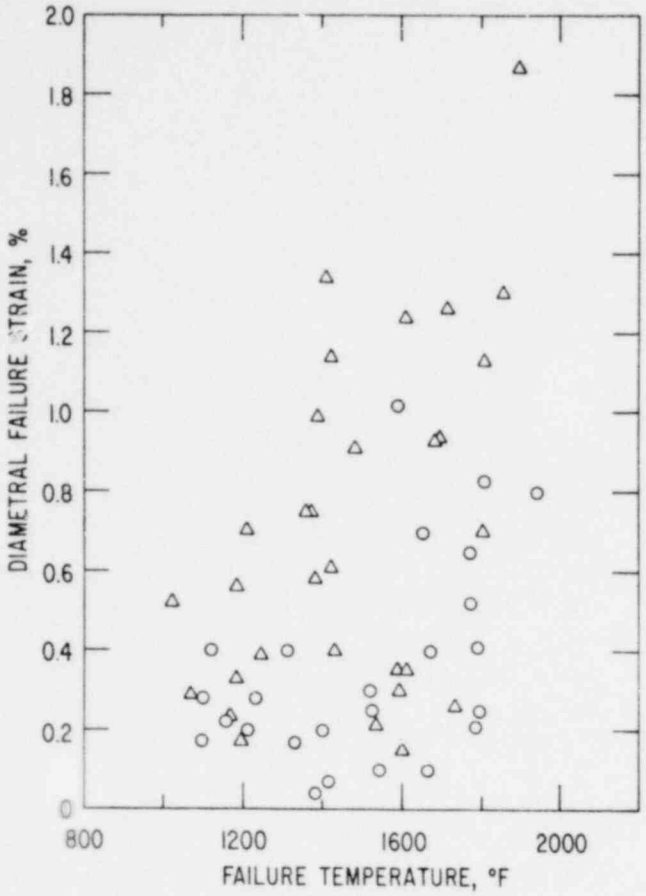

Fig. 1.

Plot of diametral failure strain vs. failure temperature for all the tests in Table I (excluding the tests 5, 9 and 22 for which the failure strain is unknown or doubtful). Circle indicates fluence in the range 2.15 - 5.82 × 10^{22} neutrons/cm^2. Triangle indicates fluence in the range 0.66 - 1.95 × 10^{22} neutrons/cm^2. ANL Neg. No. 116-79-289.

generally lower than those for the lower fluence group. Figure 2 is a similar plot of diametral failure strain against failure temperature but only the specimens with fluence in a very small range around ~1.0 × 10^{22} neutrons/cm^2 (in the range 0.85 - 1.13 × 10^{22} neutrons/cm^2) have been selected so that the possible scatter due to the dependence of failure strain on fluence is eliminated from the variation of failure strain with failure temperature. The fluence of ~1.0 × 10^{22} neutrons/cm^2 and the range of 0.85 - 1.13 × 10^{22} neutrons/cm^2 has been selected for this purpose because this is the narrowest range with a reasonable number of specimens to make a plot. It is concluded from Figs. 1 and 2 that the effect of irradiation on diametral failure strain is large enough to mask the variation of failure strain with failure temperature. The fluence which produces this dominating effect is ~1.0 × 10^{22} neutrons/cm^2 or somewhat lower.

To see the dependence of diametral failure strain on fast neutron fluence, a plot of failure strain vs. fast fluence for those 16 tests in Table IV which end in failure temperatures in the range 1665-1940°F is shown in Fig. 3. The selected tests have been limited to a range of failure temperature so that the small scatter possible due to the dependence of failure strain on failure temperature is eliminated from its variation with fluence. The highest failure temperature in Table IV is 1940°F, and this range of failure temperature is as close as possible to the failure temperature (~2000°F) at which the unirradiated cladding failure strain is maximum (when plotted against failure temperature). Most of the 16 tests plotted in Fig. 3 correspond to a gas pressure of 4 ksi, and since a particular value of gas pressure could

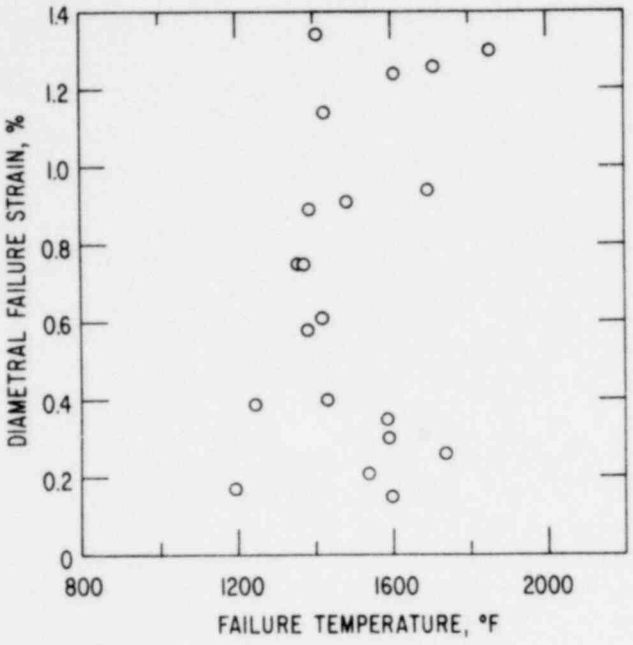

Fig. 2.

Plot of diametral failure strain vs. failure temperature for those 20 specimens in Table I which have a Fluence of ∿1.0 × 10^{22} neutrons/cm^2 (in the range 0.85 - 1.13 × 10^{22} neutrons/cm^2). These tests are: 7, 8, 12, 29 to 37, 39 to 42, and 44 to 47. ANL Neg. No. 116-79-267.

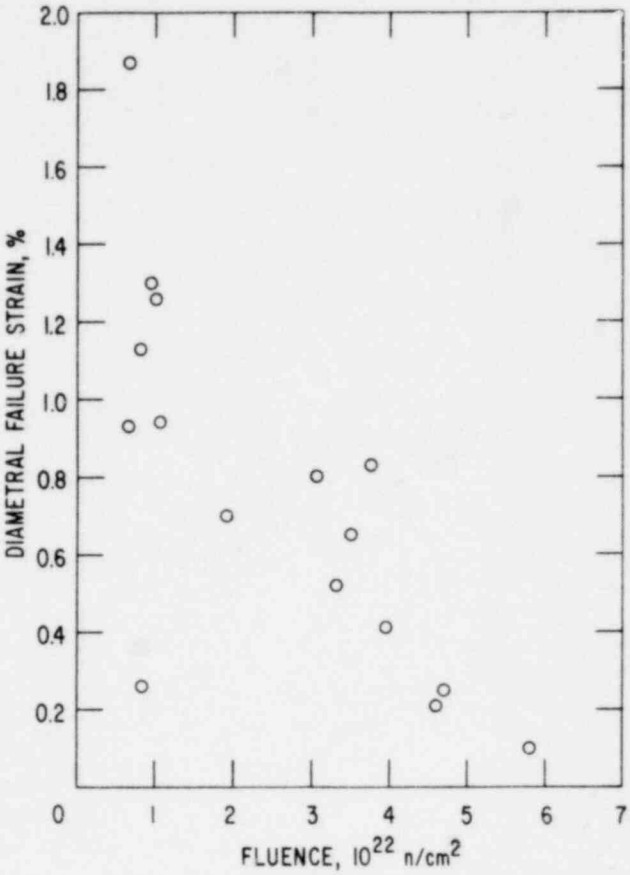

Fig. 3.

Plot of diametral failure strain vs. fast fluence for those 16 tests in Table I which are in failure temperatures in the range 1665-1940°F. This range of failure temperature is as close as possible to the failure temperature (∿2000°F) at which the diametral failure strain of the unirradiated cladding is maximum (when plotted against failure temperature). These tests are: 1, 2, 4, 6, 17, 25 to 27, 37, 42, 43, 45, 46, 48, 49 and 58. ANL Neg. No. 116-79-268.

be equivalently used instead of a particular range of failure temperature a plot of failure strain vs. fluence for those 15 specimens in Table IV which were tested at a gas pressure of 4 ksi has also been made (see Fig. 4). Except for a couple of scattered points, Figs. 3 and 4 seem to indicate that the irradiated cladding failure strain (probably its maximum with respect to its variation with failure temperature) decreases monotonically with increasing fast fluence. A pair of similar plots of failure strain against fluence is shown in Figs 5 and 6. Figure 5 includes only those 16 tests in Table IV which end in failure temperatures in the range 1020-1310°F. Most of these 16 tests correspond to a gas pressure of 10 ksi, and Fig. 6 includes only those

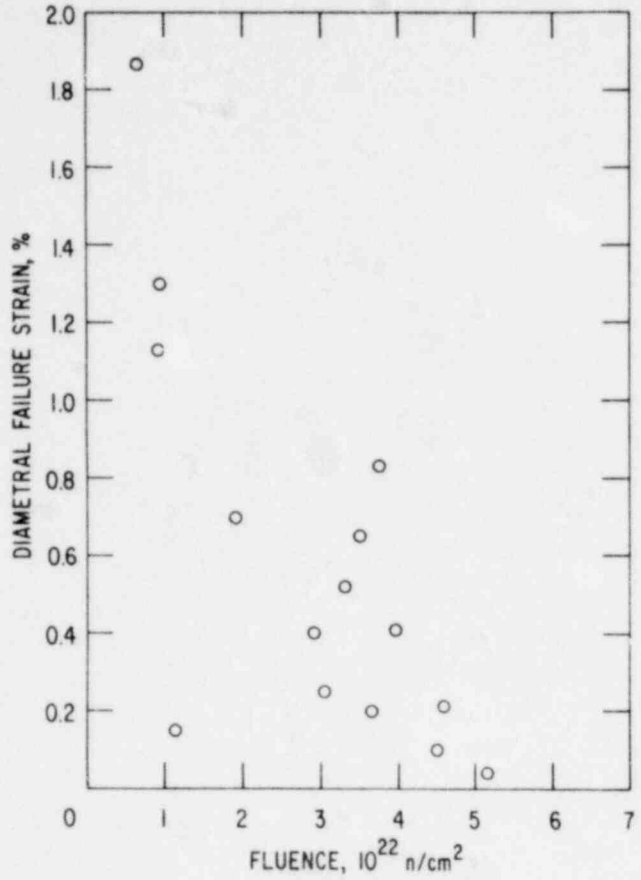

Fig. 4.

Plot of diametral failure strain vs. fast fluence for those 16 specimens in Table I which were tested at a gas pressure of 4 Ksi. Tests at this gas pressure produce failure temperatures as close as possible to the failure temperature (~2000°F) at which the unirradiated cladding failure strain is maximum. These tests are: 1, 2, 4, 6, 12 to 14, 26, 27, 42, 43, 50, 51, 58, 59. ANL Neg. No. 116-79-266.

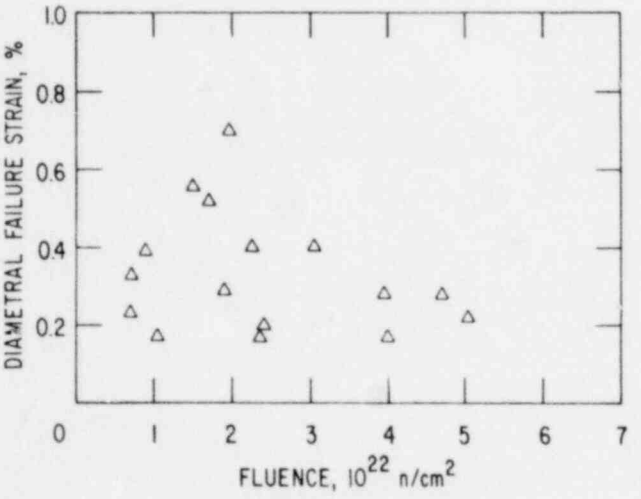

Fig. 5.

Plot of diametral failure strain vs. fast fluence for those 16 tests in Table I which end in failure temperatures in the range 1020-1310°F. These tests are: 10, 11, 16, 18, 20, 21, 28, 30, 34, 38, 53 to 57 and 60. ANL Neg. No. 116-79-279.

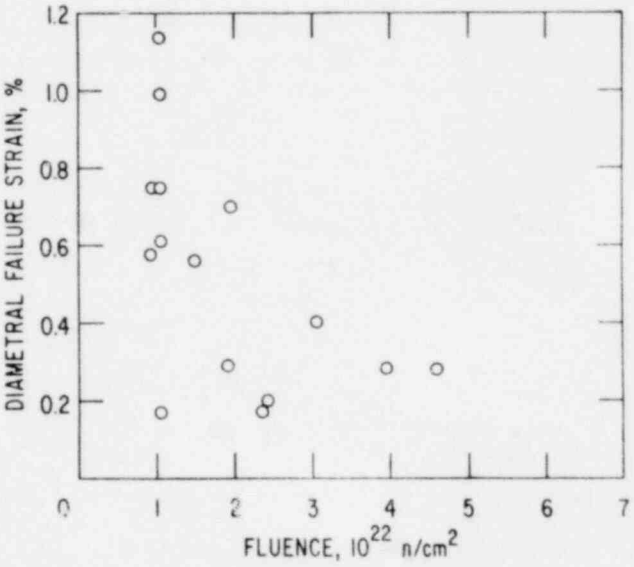

Fig. 6.

Plot of diametral failure strain vs. fast fluence for those 15 specimens in Table I which were tested at a gas pressure of 10 Ksi. These tests are: 4, 5, 6, 8, 11, 18, 20, 29 to 31, 39 to 41, 53 and 60. ANL Neg. No. 116-79-278.

15 specimens in Table IV which were tested at this gas pressure. Figures 5 and 6 seem to indicate that the irradiated cladding failure strain is scattered below a value which decreases monotonically with increasing fast fluence. The observation made from Figs. 3 and 4 is consistent with this indication. As expected from unirradiated cladding data the failure strains in Figs. 5 and 6 are generally lower than those in Figs. 3 and 4.

Figure 7 is a plot of diametral failure strain vs. fast fluence for all the tests in Table IV (excluding the tests 5, 9 and 22 for which the failure strain is unknown or doubtful). With 95% confidence, the irradiated cladding diametral failure strain ε_f could be bounded for a fluence ϕt (in units of 10^{22} neutrons/cm^2) as follows:

$$0.05 < \varepsilon_f \, \% < 1.6 - 0.25\, \phi t. \qquad (1)$$

The scatter of data is roughly uniform over this triangular region of the failure strain vs. fluence plot, and Eq. (1) is applicable only over the fluence range of the data base, $0.66 - 5.82 \times 10^{22}$ neutrons/cm^2.

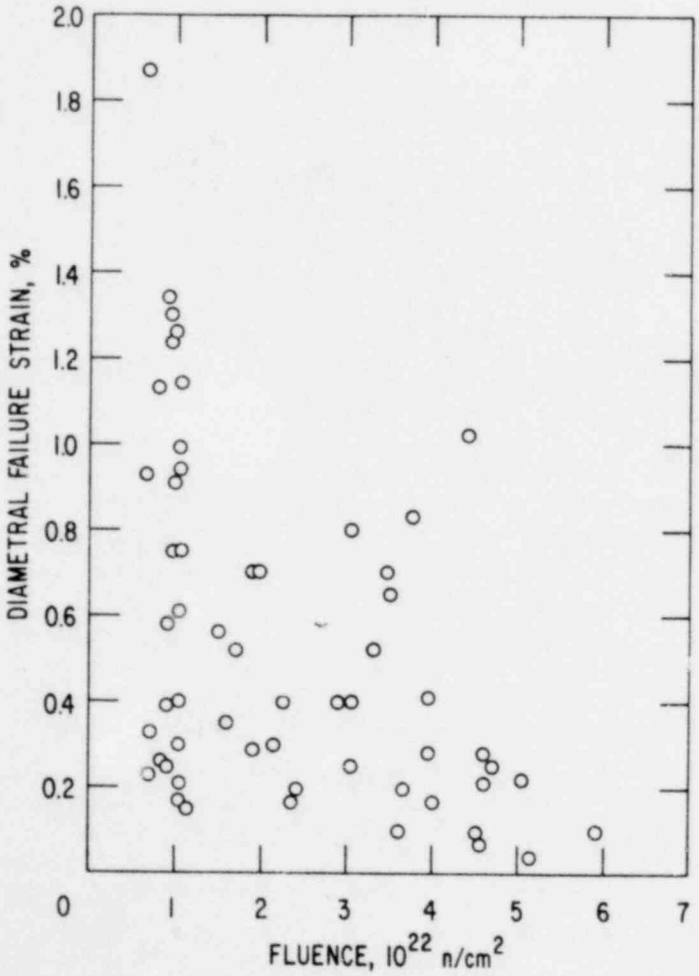

Fig. 7.

Plot of diametral failure strain vs. fast fluence for all the tests in Table I (excluding the tests 5, 9 and 22 for which the failure strain is unknown or doubtful). ANL Neg. No. 116-79-287.

This uncertainty in the failure strain makes it difficult at present to use a failure criterion based on the maximum strain theory for pin failure prediction during transient heating.

C. FRAM Development

1. BIFLO Model Development (J. J. Sienicki, P. B. Abramson, P. L. Garner and M. F. Kennedy

The BIFLO model[13] is being developed to treat the multidimensional aspects of sodium boiling within a subassembly. BIFLO (and a future model for fuel/cladding/coolant motion, FCC) will be merged with portions of the SAS4A code to form FRAM.

The current version of BIFLO will perform a steady-state initialization and perform transients which induce boiling and voiding up to initiation of dryout. A simplified fuel-pin heat transfer routine is being used during this development stage; this calculation will eventually be performed in FRAM by the TSHTR module of SAS4A. The modeling in the channel is homogeneous at the present time; there is no radial variation of quantities and no slip between sodium liquid and vapor. The models for liquid/vapor slip and for distinguishing between boiling and bypass-flow regions radially are being developed.

2. Comparison of BIFLO and SAS Codes for Steady-State and Transient Calculations without Boiling (J. J. Sienicki)

During this quarter, work was started on the programming of an initial version of BIFLO. We report here the results of a comparison between the steady state and preboiling transient portions of this initial version and those of the SAS code.

In carrying out this comparison, use was made of an existing SAS calculation for a hypothetical loss of flow scenario we are studying for a model large fast reactor. The comparison was limited to the behavior of the lead channel in this SAS calculation.

The geometry, linear power distribution, fuel and steel thermophysical properties and fluid flow/heat transfer correlations used in the BIFLO calculation were taken to be identical to those used in the SAS calculation. However, different sodium properties were used. We have chosen to work exclusively with updated sodium properties[14] while the SAS calculation relied on older sodium data.

The time dependent normalized total power, channel inlet pressure, inlet temperature, and outlet pressure (which remained constant for this problem) were obtained from the SAS run and used as "boundary conditions" for the BIFLO calculation similar to the manner in which they constitute "boundary conditions" for the SAS coolant dynamics routines.

A difference in the two calculations occurs in the determination of the heat fluxes to and from the coolant. At each axial location, SAS employs a detailed multinode radial fuel pin heat conduction calculation together with a simple single node calculation of the effect of the hex can (assumed to

transfer no heat to an inter-subassembly bypass or to other subassemblies). Although we will eventually couple BIFLO to a more detailed heat transfer calculation, the following simple heat transfer model was developed and written to facilitate immediate comparison to SAS as well as to other calculations and soidum boiling/voiding experiments. The fuel-clad-coolant heat transfer at each axial location is modeled using only one node in each of the fuel and clad coupled by appropriate thermal resistances. The resulting equations which couple the fuel, clad, and sodium coolant temperatures are time centered and sovled implicitly by a) first performing a forward elimination to eliminate the fuel and clad temperatures in terms of the coolant temperature for all axial levels; b) performing all fluid dynamics calculations (including the determination of the coolant temperatures implicitly coupled to the eliminated clad temperatures); c) back substituting the coolant temperature to obtain the clad and fuel temperatures. This solution strategy for implicitly coupling fluid dynamics and heat transfer calculations is similar to the one used in TRAC[15] and THERMIT[16] and avoids the necessity of using much reduced time steps in order to eliminate numerical difficulties encountered when an explicit coupling is attempted (e.g., as in COBRA IV[17]).

A similar two-node treatment is also used at those axial portions of the pin containing insulator pellets or gas plenum. Any number of pins may be defined for a given coolant channel to better account for the effects of incoherencies following boiling initiation. Furthermore, a two-node treatment is also used to account for the heat transfer effects of surrounding subassembly hex can/insulator/flow-bypass geometry. For the present problem, the hex can was represented by both nodes and no heat transfer was permitted into the inter-subassembly bypass.

The steady-state temperature and pressure profiles obtained with BIFLO and SAS are shown in Figs. 8 and 9 where it is seen that excellent agreement is obtained between the two calculations. We note here that for both codes the details of the heat transfer routines play no role in determining the coolant steady state (since all of the fission energy is removed by the coolant in steady state). In addition to the temperatures and pressures, a quantity of significance in comparing calculations is the mass flowrate (or flux) for the channel. The mass flux is calculated by BIFLO to be 587.6 g/cm^2-s compared with 593.2 g/cm^2-s obtained by SAS. Again, this is excellent agreement. A possible explanation for the slight differences between results from the two codes could be the use of different sets of sodium properties.

Excellent agreement is also obtained between BIFLO coupled to our simple heat transfer model and SAS as the preboiling phase of the flow coastdown is followed out with the two codes from their respective steady states. Figures 10 and 11 show the temperature and pressure profiles 17.7 s after the coastdown is initiated. At this time, the mass flux calculated by BIFLO is 192.2 g/cm^2-s compared with 196.1 g/cm^2-s obtained by SAS. Again, the small differences between the results of the two calculations are very likely a consequence of the use of greatly different heat transfer calculations as well as the use of different sets of sodium properties (which exhibit greater deviation from one another as the temperature is increased).

In addition to showing that the steady state and preboiling portions of BIFLO have been programmed correctly, the present calculation demonstrates BIFLO's capability to efficiently calculate incompressible thermohydrodynamics

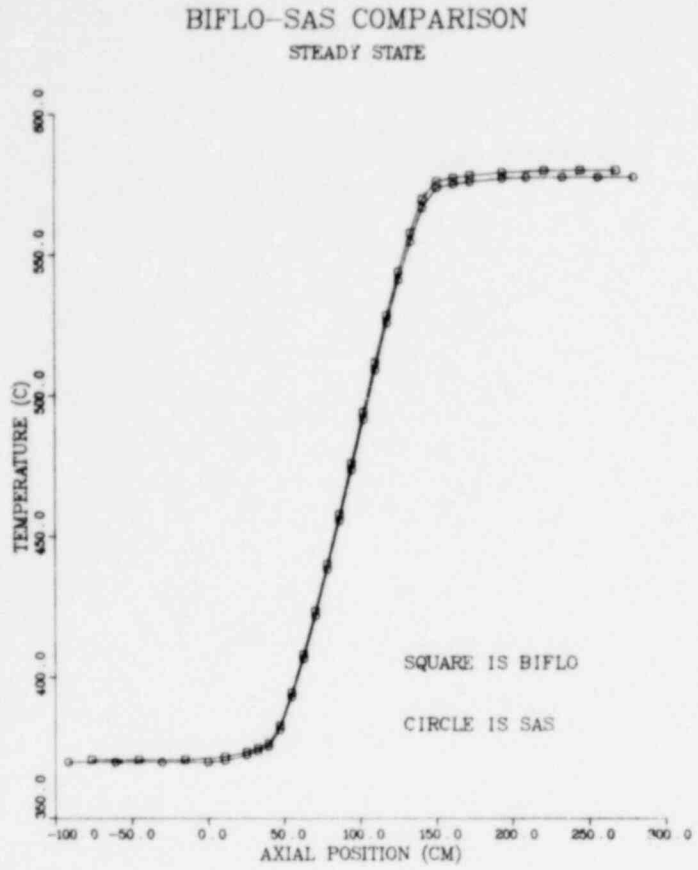

Fig. 8.

Comparison of Steady State Temperature Calculated with BIFLO and SAS. ANL Neg. No. 116-79-273.

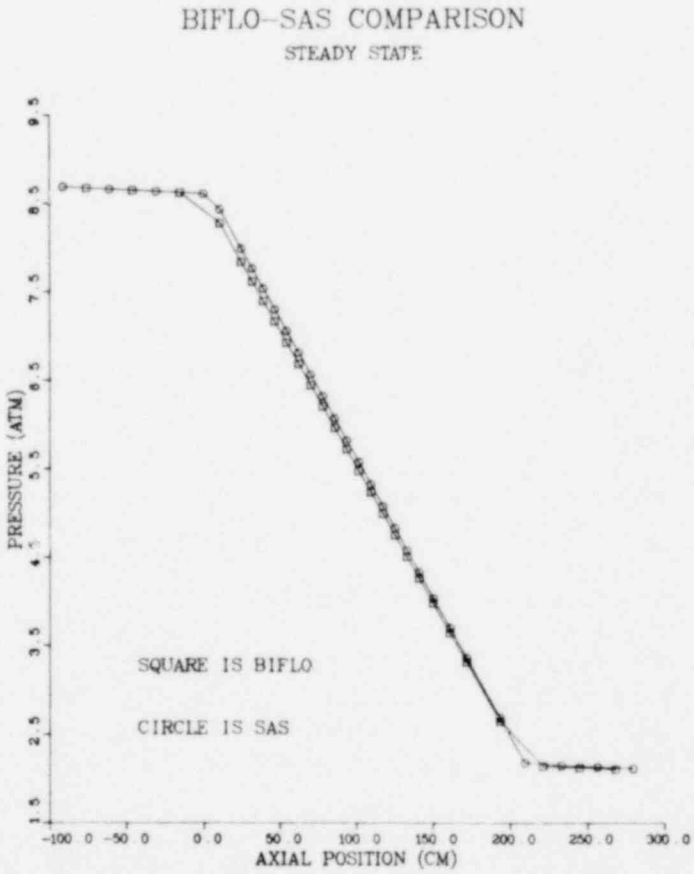

Fig. 9.

Comparison of Steady State Pressures Calculated with BIFLO and SAS. ANL Neg. No. 116-79-271.

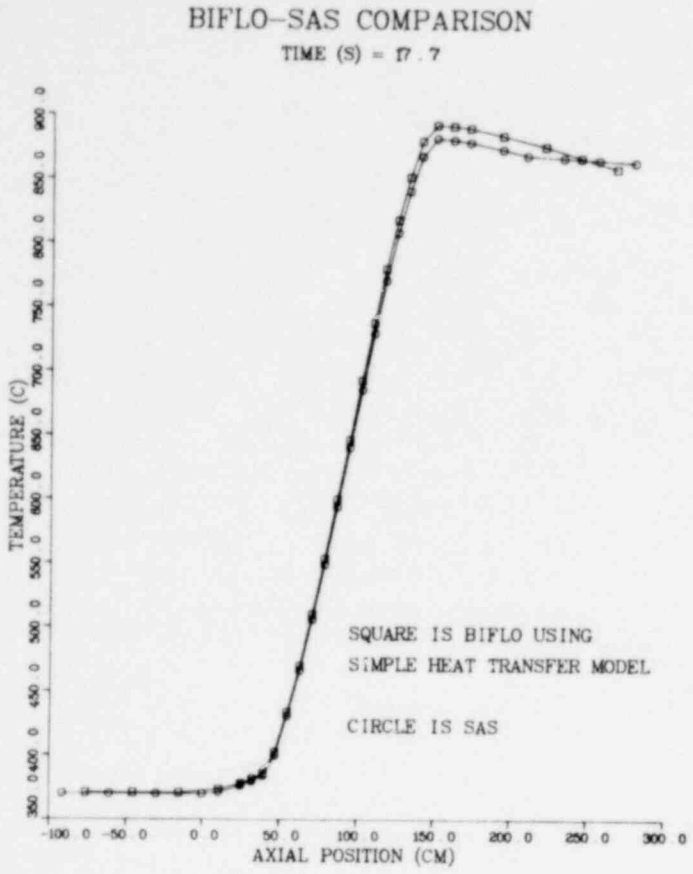

Fig. 10.

Comparison of Temperatures Calculated with BIFLO Coupled to a Simple Heat Transfer Model and SAS at 17.7 s. ANL Neg. No. 116-79-272.

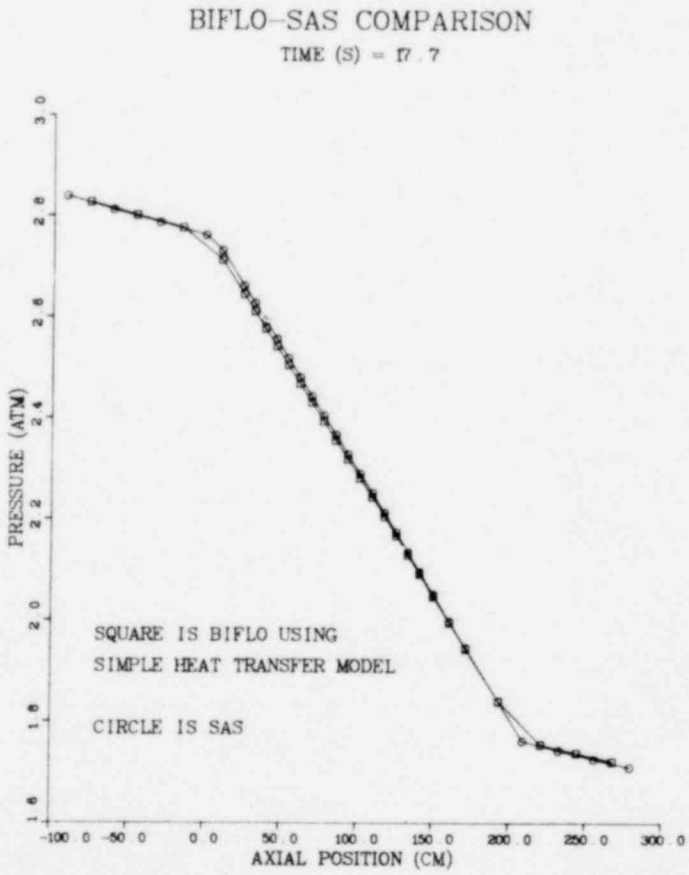

Fig. 11.

Comparison of Pressures Calculated with BIFLO Coupled to a Simple Heat Transfer Model and SAS at 17.7 s. ANL Neg. No. 116-79-269.

over time scales of the order of tens of seconds. For the BIFLO calculation, time steps of 0.1 s were employed (which initially exceed the Courant limit defined by U. $\delta t/\delta z = 1$ by a factor of about ten). Continuing efforts address the efficient calculation of the boiling phase of this transient.

3. BIFLO Benchmark Capability (M. F. Kennedy)

Various multidimensional thermal hydraulics computer programs were reviewed to determine which programs could provide a numerical benchmark capability for the BIFLO modeling effort. The COMMIX-2 program,[18] the COBRA-IV program,[17] the UK SABRE[19] code and the MIXING[20] code were all considered for this task. Each of these programs can provide some measure of a benchmark capability with COMMIX being the best followed by COBRA IV and SABRE and then MIXING. A transient two phase version of SABRE however will not be available to users for at least another year. The COMMIX-2 program which is still undergoing major revisions is capable of providing the desired benchmark capability. However, after discussions with the developers of COMMIX, it was decided to wait unitl the modifications to improve the calculational speed of the program are completed. Efforts have, therefore, been directed toward implementing the COBRA-IV and MIXING codes.

COBRA-IV has the capability to provide a detailed analysis of the steady-state and transient thermal hydraulic conditions in a nuclear reactor fuel rod bundle, including the ability to follow the problem through boiling and flow reversal. COBRA-IV can provide information on the fluid and structure temperature fields in addition to providing information on the axial and radial propagation of the boiling event within a subassembly. This will provide the necessary near term benchmark capability and will also provide information to guide the modeling effort as it progresses. COMMIX-2 will be used as a long-term benchmark capability.

The MIXING code was obtained from Chen and Ishii (ANL/RAS). This code employs an R-Z model and treats the boiling zone like a growing blockage, forcing flow to bypass the boiling region. Although the models are inadequate for the problem to be studies with BIFLO, this code will be useful to assess the boiling region growth rate, the bypass flowrates and the fuel pin and coolant temperature gradients. The MIXING code has been implemented and a number of sample problems have been run.

A number of COBRA calculations have been completed for a flow coastdown transient in a 37 pin bundle using an ANL/RAS version of the COBRA-IIIC program.[21] These transients were terminated just prior to boiling inception, but they do provide a characterization of the temperature and flow conditions in the bundle from steady state conditions up to boiling inception.

Efforts have been initiated to obtain the latest version of the COBRA-IV program which will allow calculations to be continued through boiling and into flow reversal.

4. Incipient Boiling Superheat in Sodium (B. A. Greer, P. B. Abramson and A. A. Kovitz)

An extensive survey of the literature on incipient boiling superheat (IBS) in sodium has been completed.[22] The survey was undertaken in the light of the possible importance of IBS upon the course of an LMFBR accident; therefore it could play an important role in reactor safety codes used for boiling and voiding. The goal was to determine if a consensus existed in the literature covering the values of IBS in sodium, the parameters influencing those values, and its importance in prototypic reactor accidents.

The study reinforced earlier reviews of IBS which concluded that many real and/or apparent experimental parameters influence IBS; this has resulted in a broad spectrum of superheat values (ranging from zero to several hundreds of degrees Fahrenheit). The significant parameters appear to be:

- inert gas concentration in the sodium,
- oxide concentration in the sodium,
- system pressure,
- pressure-temperature history of the system,
- rate of temperature rise,
- heat flux,
- coolant flowrate,
- operating time on the system,
- surface conditions of the coolant channel,
- nuclear radiation.

Much of the reported experimental data is not only scattered but sometimes contradictory since the large number of operating parameters are difficult to control. Therefore, no comprehensive theory for IBS exists which can reveal the relative importance and/or the fundamental nature of the variables studied to date. However, workers agree that inert gas and oxide concentrations are the two most influential parameters; their magnitudes, moreover, appear to be closely related to the pressure-temperature history of the system.

The basic requirement for transition from single phase liquid to boiling heat transfer is the existence of bubble nucleation sites. These sites may be within the bulk phase as vapor bubbles and/or oxide particles; they are also present as surface cavities within which vapor or inert gas pockets exist. The magnitude of IBS depends upon the number and nature of such sites. Any operating condition which promotes the existence of favorable nucleation sites will reduce IBS; operation that tends to eliminate them will increase IBS. This relatively simple criterion is complicted by any dynamic influences such as rate of temperature rise, heat flux and flow rate, these are among the more difficult parameters to access.

Of crucial importance to the question of IBS is the prototypic nature of the experiments. It is argued that an operating reactor is not likely to exhibit significant superheat due to its pressure-temperature history. Such a reactor, with its many interconnecting flow paths and large,

agitated, cover-gas/coolant interface, is likely to have a significant concentration of inert gas and oxides in the bulk coolant as well as many active superficial nucleation sites at any instant when a coolant flow-power mismatch might arise. Furthermore, it is argued any superheat which may exist will not be important during a large excursion involving significant temperature variations. This scenario suggests that IBS may be a negligible parameter in prototypic boiling and voiding codes. Experiments in which the pressure-temperature history has been carefully controlled do support the comments noted above.

However, other experiments (both past and current) exhibit significant IBS in liquid sodium. This superheat certainly influencies the course of a boiling and voiding occurance. Any code meant to model these experiments must include IBS as a parameter.

Experimental superheat data reported from different labs are often contradictory. Inert gas concentration is generally agreed to be a very significant parameter; it has been postulated to be responsible for the heat flux and velocity effects. Unfortunately, very few investigators control or measure the inert gas concentration and thus its true effect is still not known. Oxide concentration is also seen as an important variable. Heat flux and rate of temperature rise show the least experimental agreement and are the least understood effects. More experimental work needs to be done to see if heat flux and rate of temperature rise are really independent variables or if their observed effects are actually due to variations in some other system parameter. The existing superheat data is not conclusive enough to be able to predict superheats for a given set of operating conditions.

5. EPIC and SAS3D/EPIC Development (P. A. Pizzica and P. L. Garner)

The distributed particle-in-cell treatment for fuel in the coolant channel in EPIC has been incorporated into SAS3D/EPIC. Two quanities associated with solid fuel in the pin have been extended to be functions of radius in EPIC: the mass of fuel per node (GMPN) and the amount of fission gas per node (FGFUF). The momentum flux term has been corrected to be $U \cdot VU$ rather than VU^2. A model has been added to treat cells in the pin which become overcompacted during the calculation; the treatment uses a "chewing gum" technique to conserve momentum. A compressible treatment of the sodium coolant slugs has been incorporated (as an option) in a version of EPIC being used for analysis of experiments.

A documentation package for EPIC is being prepared. As a part of the effort, comment statements have been added throughout he code, obsolete coding has been removed, some calculational sequences have been reorganized, and the input and output requirements have been improved. A users' guide is in preparation.

D. Consultations and Cooperative Studies

1. Results for the WAC 1$/s TOP Study for a BOL Core using SAS3D/EPIC (P. A. Pizzica and H. H. Hummel)

The SAS3D/EPIC[23,24] code has been used for the USNRC contribution to the TOP calculations for the comparative study group. The data for the

calculations come from WAC-D-68[25] for the reactor model and from WAC-D-77[26], 82[27] and 85[28] for the TOP specifications.

Modifications to SAS3D/EPIC

It was decided that certain modifications should be made to make the SAS3D/EPIC calculation conform to the ground rules of the study and to reduce somewhat the differences introduced into the results by inconsistencies between the other FCI models and EPIC.

The study assumptions require that a fixed amount of fuel be removed from the molten fuel cavity in the pin at the time of pin failure and the rate of heat transfer from this fuel to sodium be fixed. Since the ejection model in EPIC could not be used, fuel in the pin cavity was cut off from any communication with the coolant channel, and the size of a clad rip at failure and its possible extension with time were issues not addressed in the study. It should be noted that the present model of EPIC would not have predicted any fuel ejection with the specified pin failure conditions.

Since it was assumed in this study that there would be no fuel motion reactivity feedback before disassembly, the pin hydrodynamics become irrelevant to the calculation prior to disassembly. However, the main contribution to such feedback would have come from fuel motion in the channel. In order to avoid spurious effects from fuel motion reactivity feedback in the disassembly phase, the "ejected" fuel was taken uniformly from the pin cavity in order to preserve a constant axial density rather than from the center nodes at which the fuel is placed in the channel. This, of course, has no immediate effect since the fuel reactivity is normalized to zero at switchover. The neutronic effects of this assumption were eliminated by renormalizing the fuel reactivity to zero at switchover time.

To conform to the study assumptions, the factor in EPIC which reduces the fuel to coolant heat transfer in the channel according to increasing coolant void fraction was removed and multiplicative factors for modeling the gradual mixing of fuel and sodium (replacing in EPIC the gradual ejection of fuel) and for the variation of the temperature gradient in the particle, both part of the Cho-Wright[29] model, were added.

Furthermore, no condensation of sodium or fuel vapor was allowed in the coolant channel.

One of the most significant changes to EPIC involved the treatment of single-phase pressures in the coolant channel subsequent to pin failure. EPIC was designed to model burst failure conditions where the coolant chanel is pressurized at pin failure and the burst pressure results from fission gas and/or fuel vapor. The present version of EPIC cannot model the single-phase pressures (which result from the melt-through conditions specified for this study) due to the thermal expansion of liquid sodium subjected to quite high heating rates in an initially unvoided sodium channel. (A future version of EPIC will be able to treat this.) In the present study, these single-phase pressures contribute to the production of quite high sodium voiding ramp rates

in the channel and thus cannot be neglected. For the purpose of this study, an artificial pressure was introduced into the coolant channel which corresponds to the acoustic-phase pressure during the first two milliseconds after pin failure from the results reported for the KiK CAPRI calculation.

Inconsistencies Between SAS3D/EPIC and the Other Codes

The study assumptions do not allow fission heating of fuel in the coolant channel or the effect of the chilling of fuel in the channel on the Doppler reactivity. EPIC violated these rules and included these effects.

A major difference between EPIC and the other codes is EPIC's Eulerian node structure in the interaction zone in the coolant channel. This detailed treatment of the fuel and sodium convection and heat transfer leads to significant differences with the other codes which treat the interaction zone as one homogenized mixing zone. This node-by-node detail in EPIC causes significant deviation from the mass ratio of fuel to sodium stated in the assumptions, which may contribute in part of the FCI zone to the much higher sodium temperature and pressures than attained by the other codes. The sodium temperature and pressure can be reduced in the nodes at the lower end of the FCI zone due to the cold sodium convecting in from the bottom of the zone prior to flow reversal, but more importantly due to the penetration into the single-phase region by the fuel particles (which in the bottom of the zone are moving faster than the lower sodium slug while in the upper part of the FCI zone the upper slug is moving faster than the fuel). Three things contribute to the lower velocity of the lower sodium slug: its greater mass, its initial positive velocity and the resistance to expulsion caused by the inlet orficing.

Another difference is that EPIC specifically calculates the feedback due to sodium voiding (which is the driving reactivity at switchover) during the disassembly phase since there is no switch to a different code at the "switchover" point, whereas in the 2-D disassembly codes the driving reactivity must be input as some function of time. Thus the reactivity feedback due to what is essentially fuel-sodium slip is explicitly calculated in EPIC and included in the two-code calculations only by superposition onto the disassembly phase of an extrapolated ramp based upon the calculational history with the first code.

EPIC does not include single-phase pressures (caused by melting and by thermal expansion), a major difference with the other codes. Since single-phase pressures become important in a VENUS-type disassembly code in areas of the reactor where the void fraction is low, this phenomenon is a major factor in producing the material motion requisite for shutdown in 2-D codes such as VENUS. In fact large single-phase pressures are seen in the two-code calculations. The displacement reactivity calculated by EPIC is produced by fuel moving within the clad under its own axial vapor pressure gradient and also by fuel moving in the coolant channel. Both the fuel in the pin and in the channel are in motion at switchover. Almost all of the initial shutdown reactivity in this calculation was from fuel motion in the channel, however.

Equations of State

Sodium:[30] T<1600°F:

$$\log_{10} P_{sat}(atm) = 6.4818 - \frac{10020.6}{T_{sat}(°R)} - 0.5 \log_{10} T_{sat}(°R)$$

1600°F<T<2500°F:

$$\log_{10} P_{sat}(atm) = 6.83770 - \frac{9980.94}{T_{sat}(°R)} - 0.61344 \log_{10} T_{sat}(°R)$$

2500°F<T<2733°K:

$$\log_{10} P_{sat}(atm) = 1.36041 - \frac{8178.27}{T_{sat}(°R)} + 0.789 \log_{10} T_{sat}(°R)$$

Fuel:[31]

$$P_{sat} = \exp(69.979 - 76800. \times \frac{1}{T}) \cdot T^{-4.34}$$

where P is in dynes/cm^2 and T in °K

Results for the Pre-Failure Phase (Table V and Figs. 12-14)

The input driving reactivity is 1$/s. This produces a power rise which causes a ramp rate from Doppler about equal to the input a second or so after initiation. The density changes in the coolant produce a slight positive ramp and net ramp rate is 22¢/s at 1 s after initiation at which time the average fuel temperature at the peak node has risen almost 400°C. Fuel melting begins about 20 ms later when the power is about 4 times nominal.

Conditions at Pin Failure

The assumed criterion for pin failure in this study is 0.6 melt fraction. This is reached at 1.842 s after initiation in the peak channel, 2, when the normalized power has risen to 11.5, the energy release is 15,669 MJ and the peak mean fuel temperature has risen about 1400°C over its steady-state value. The net reactivity is 75¢ but the Doppler has brought the net ramp rate down to 9¢/s.

Channel 3 fails about 1.8 ms after 2 but channel 4 doesn't fail until about 8.7 ms after channel 2 and channels 5, 6, 7 all fail before switchover between 10 and 10.4 ms after first failure. Channel 8 fails a few tenths of a millisecond after switchover.

TABLE V. 1$/s TOP for the "Europe" Reactor - SAS/EPIC Results

Steady State Results	Nominal Reactor Power	MW	1947
	Maximum Linear Power	W/cm	450
	Peak Fuel Center Temperature	°C	2442
	Peak Mean Fuel Temperature	°C	1600
	Coolant Outlet Temperature	°C	611
Conditions After 1 s	Normalized Power	-	3.8
	Net Reactivity + Ramp	$, $/s	0.63, 0.22
	Doppler Reactivity + Ramp	$, $/s	-0.414, -0.90
	Void Reactivity + Ramp	$, $/s	0.043, 0.12
	Period	s	0.83
	Peak Mean Fuel Temperature	°C	1983
Start of Fuel Melting	Time	s	1.0[illegible]
	Energy Release	MW·s	4429
	Peak Mean Fuel Temperature	°C	2006
Condition at Failure	Failure Time	s	1.842
	Energy Release	MW·s	1566[illegible]
	Normalized Power	-	11.46
	Period	s	0.67
	Net Reactivity + Ramp	$, $/s	0.746, 0.09
	Coolant Temperature at Top of Active Zone	°C	930
	Peak Mean Fuel Temperature	°C	2994
Failure Sequence	Channels	-	2/3/4/5/7/6/8
Onset of Core Disassembly	Time	s	1.853
	FCI Time	ms	10.9
	Normalized Power	-	1806
	Period	s	0.00093
	Energy Release	MW·s	18963
	Energy Release after Failure	MW·s	3294
	Energy of Molten Fuel	MW·s	2410
	Mass of Molten Fuel	kg	5046
	Net Reactivity + Ramp	$, $/s	1.131, -136
	Doppler Reactivity + Ramp	$, $/s	-1.473, -225
	Void Reactivity + Ramp	$, $/s	0.750, +88

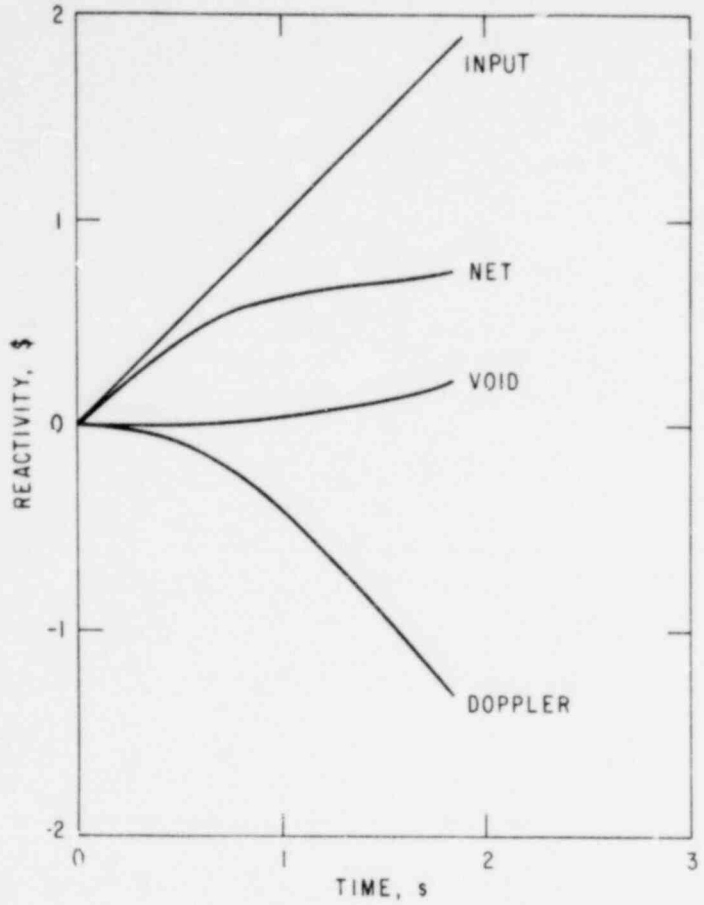

Fig. 12.

Reactivity Histories for 1 $/s TOP WAC Study. ANL Neg. No. 116-79-288.

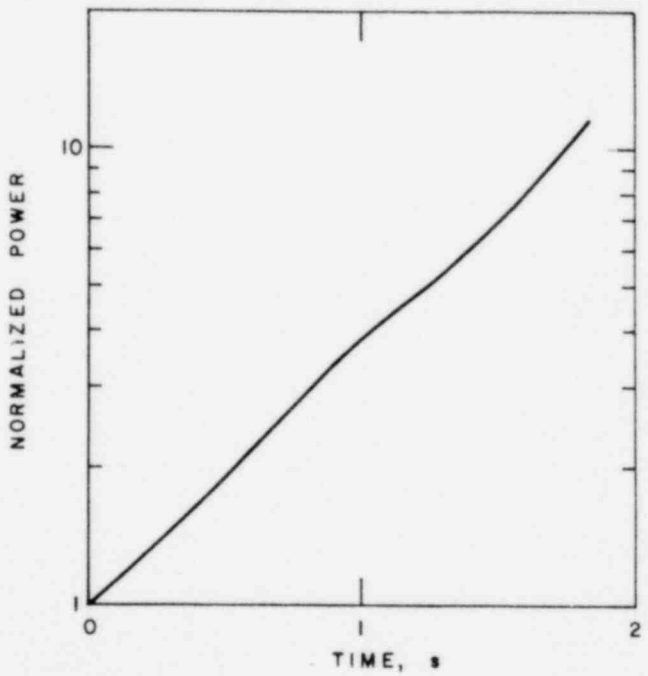

Fig. 13.

Normalized Power vs. Time for 1 $/s TOP WAC Study. ANL Neg. No. 116-79-284.

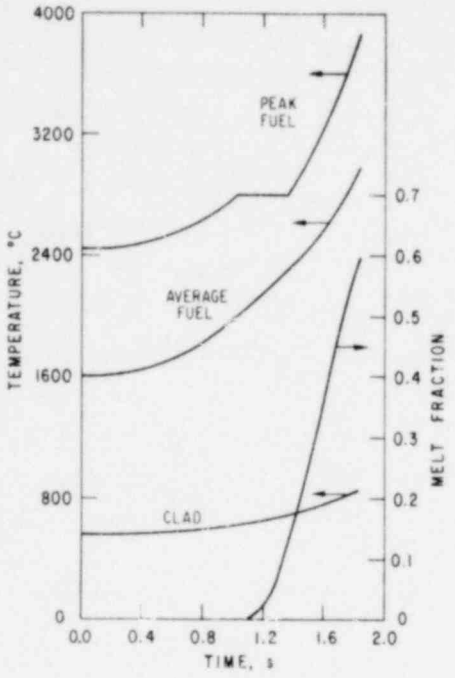

Fig. 14.

Temperatures and Fuel Melt Fraction for Ch. 2 vs. Time for 1 $/s TOP WAC Study. ANL Neg. No. 116-79-276.

Results of the FCI Phase (Tables V - VI and Figs. 15-20)

The study assumptions specify that an amount of fuel equal to six times the amount of sodium in a 10 cm length at the midplane be placed in the channel at pin failure and that displacement effects are to be neglected. This amounted to 12.06 g of fuel per pin for EPIC. The temperature of this fuel is taken to be the average temperature of the molten fuel at the core midplane which is 3471°C for channel 2. This fuel is uniformly removed from the fuel cavity so that every axial node in the molten fuel cavity has the same density after fuel ejection.

The present model of EPIC was written to compute conditions after a burst failure and the melt-through conditions specified for the current study presented a problem for the code in the calculation of the single-phase pressures due to thermal expansion of the sodium. No mechanistic calculation of this acoustic phase was attempted but a fixup was put in the code to override EPIC's normal pressure calculation with the acoustic-phase pressures reported in the CAPRI calculation. More precisely, an approximation to the CAPRI pressure curve was put in with three linear fits which brings the pressure to a peak of 114 atm at 1.4 ms FCI time and declines to 10 atm at 2.0 ms where the vapor pressure curve from the sodium crosses the acoustic pressure curve and surpasses it. 2.0 ms is therefore the point at which "boiling" begins. The pressure curve given for the FCI zone in Figure 16 is the maximum pressure in the FCI zone and there can be considerable variation over the zone, especially as the zone expands with time. Because of the high heating rate and perhaps because of the deviation from the mass ratio and EPIC's non-homogenized FCI zone approach, as explained above, the maximum sodium temperature is calculated to reach the critical point and is artificially held fixed just below it.

TABLE VI. FCI Results (Channel 2) from SAS/EPIC for 1$/s TOP WAC Study

FCI Initiation	Time		s	1.842
	Axial Failure Position		%A.L.	50
	Initial Length of FCI Zone		m	0.10
	Fuel in FCI	-Mass	g	12.06
		-Temp	°C	3471
	Sodium in FCI	-Mass	g	2.01
		-Temp	°C	715
FCI Results	Max. Single-Phase Sodium Press		bar	114
	Start of Sodium Vaporization		ms	2.0
	Max. Sodium Vapor Pressure		bar	391
Condition After 8 ms of FCI	Interface Position	-Upper	m	2.05
		-Lower	m	1.55
	Interface Velocity	-Upper	m/s	103.2
		-Lower	m/s	-36.2

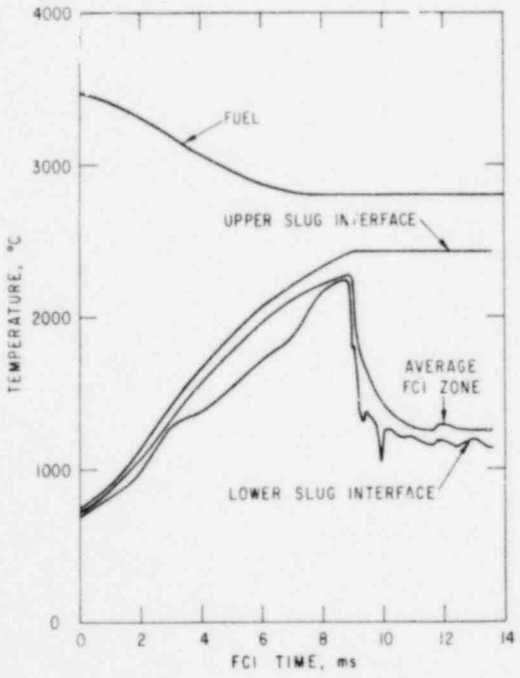

Fig. 15.

Channel Fuel and Sodium Temperatures (Ch. 2) vs. Time after FCI Initiation for 1 $/s TOP WAC Study. ANL Neg. No. 116-79-274.

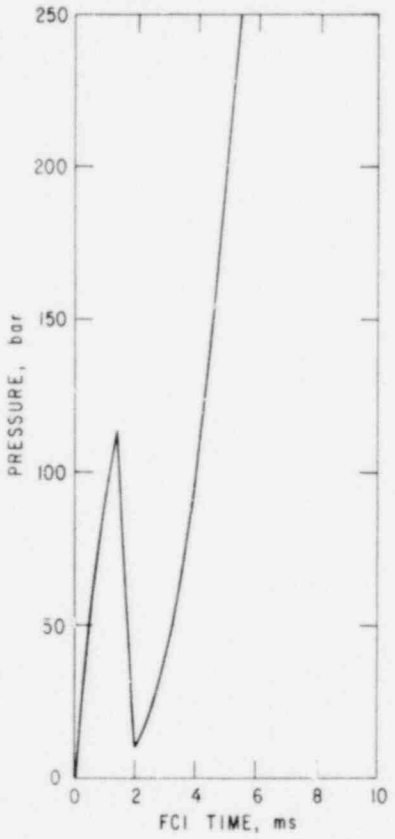

Fig. 16.

Maximum FCI Zone Pressure (Ch. 2) vs. FCI Time for 1 $/s TOP WAC Study. ANL Neg. No. 116-79-275.

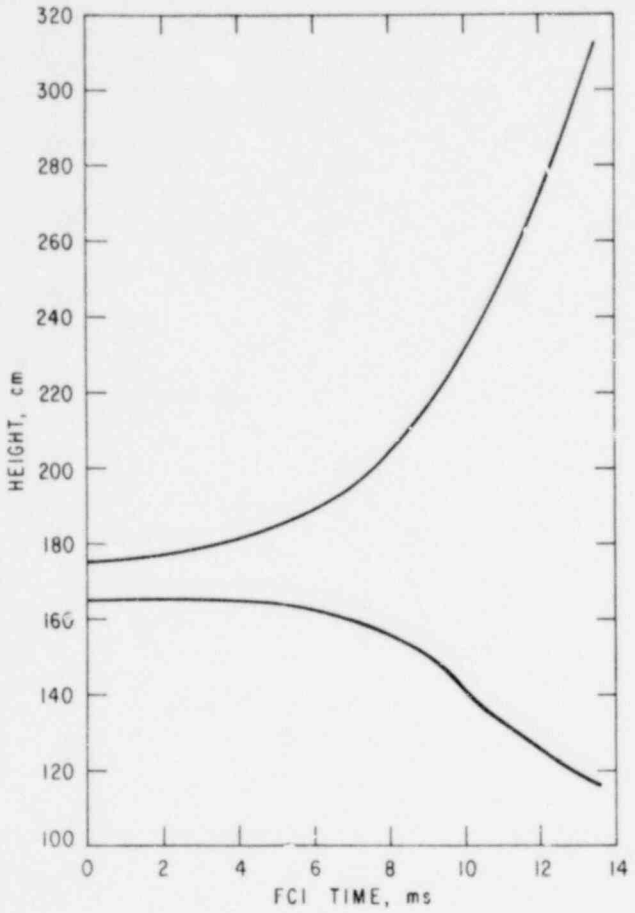

Fig. 17.

FCI Zone Boundaries vs. FCI Time (Ch. 2) for 1 $/s TOP WAC Study. ANL Neg. No. 116-79-277.

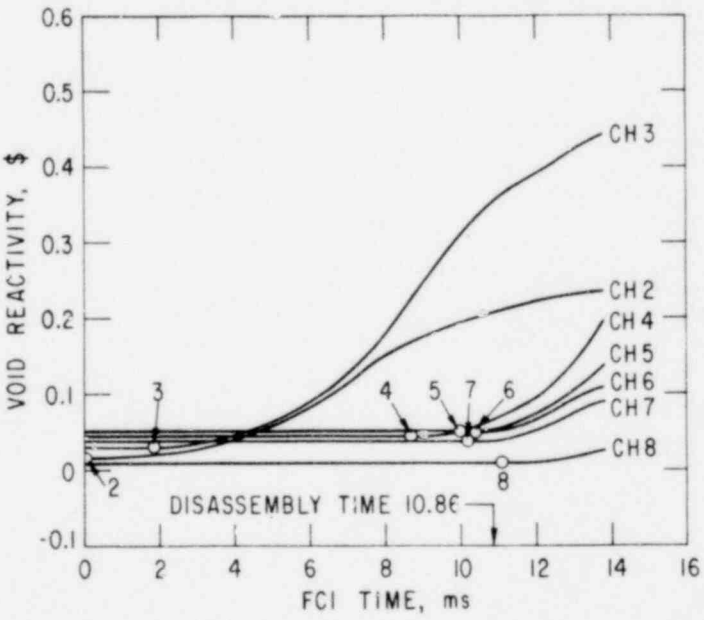

Fig. 18.

Void Reactivities vs. FCI Time for 1 $/s TOP WAC Study (Circle on curve denotes failure.) ANL Neg. No. 116-79-293.

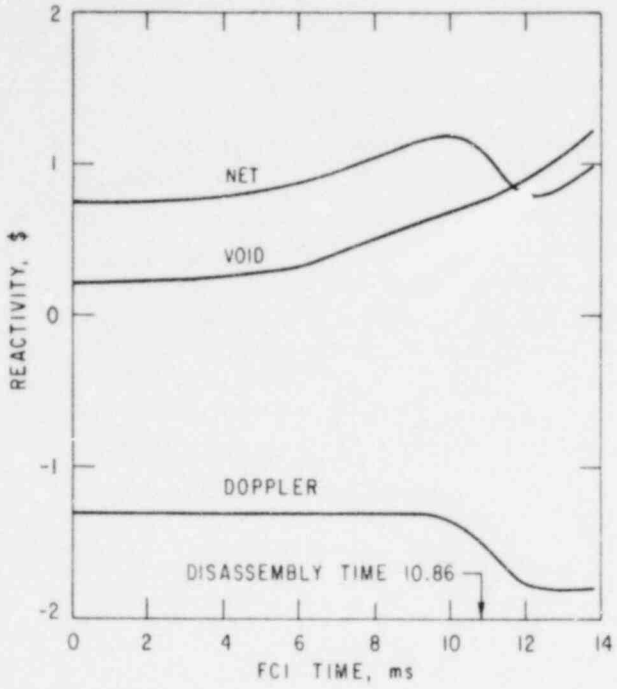

Fig. 19.

Reactivities vs. FCI Time for 1 $/s TOP WAC Study. ANL Neg. No. 116-79-292.

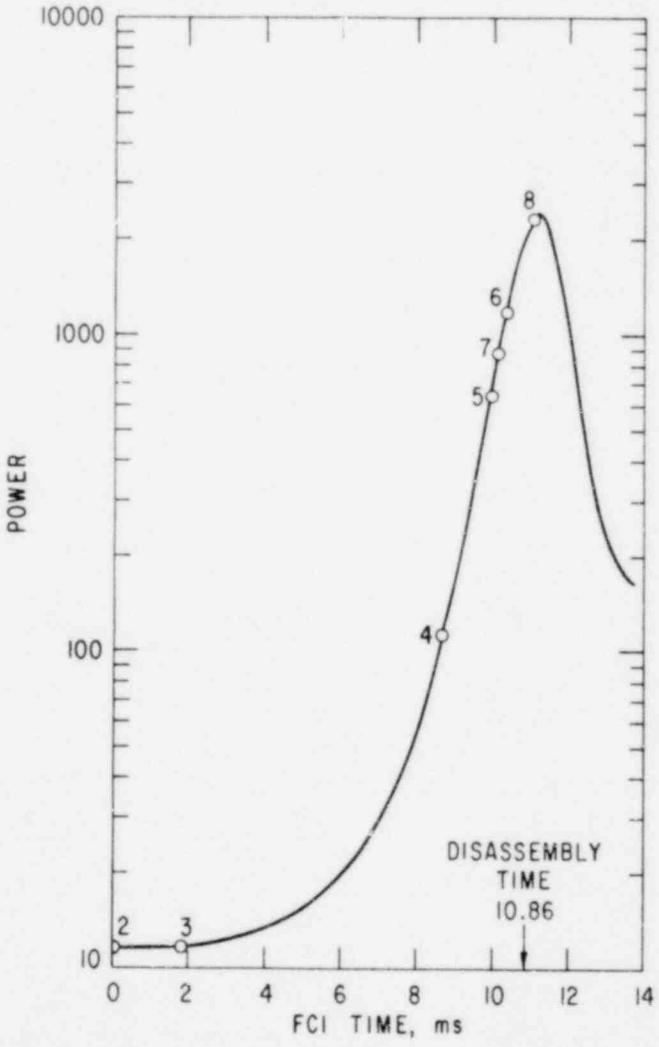

Fig. 20.

Normalized Power vs. FCI Time for 1 $/s TOP WAC Study (Circle on curve denotes channel failure). ANL Neg. No. 116-79-291.

The fuel temperature in Fig. 15 is seen to fall to the melting point and then stay there for the remainder of the calculation. In the present version of EPIC, fuel is allowed to go below the melting point, but the heat of fusion has not been lost by the end of the computation. The sodium temperature in Fig. 15 requires some explanation. The upper sodium slug velocity stays ahead of the advancing fuel particles moving upwards which preserves a rather higher fuel/sodium mass ratio and the critical temperature in the sodium is reached after 9 ms. The mass ratio is rather lower for the fuel which moves downwards in the channel and this prevents quite as rapid a heat-up of the sodium although the temperature at the lower slug interface peaks at over 2200°C and then declines rapidly as the fuel particles moving downward penetrate the lower slug (in EPIC, the farthest advance of the fuel particles defines the FCI zone boundaries if they move beyond the slug interface), which reduces the sodium temperature at the lower slug interface and the corresponding channel pressure as well as the FCI zone average sodium temperature as more cold sodium is brought into the zone. These considerations indicate that the sodium temperatures from the EPIC calculation cannot be compared in a meaningful way with those from a homogenized calculations after a certain stage in the analysis.

Conditions at Onset of Disassembly Phase (Table V and VII and Figure 21)

"Switchover" to the disassembly phase (which for EPIC meant continuing essentially the same calculation but allowing fuel motion feedback) was specified at a peak node average temperature of 3300°C. This occurred at 10.9 ms after first failure and at a normalized power of 1806 with an energy release of 18963 MJ (with 3294 MJ added after first failure). About 34% of the core fuel inventory is molten with an energy of 2410 MJ (relative to solidus).

TABLE VII. Condition at Onset of Disassembly for 1$/s TOP WAC Study

			2	3	4	5	6	7
Int. Pos.	-Upper	m	2.47	2.16	1.77	1.76	1.75	1.76
	-Lower	m	1.34	1.52	1.65	1.65	1.65	1.65
Int. Vel.	-Upper	m/s	199.1	132.2	18.1	9.2	7.1	8.0
	-Lower	m/s	-36.8	-44.0	-0.6	4.8	5.5	5.1
Void Ramp Rate		$/s	12	45	22	5	1	2

The voiding feedback from channels 2 and 3 dominate at the time of switchover although channel 4 is contributing one quarter of the total sodium ramp rate at that time but far less in total reactivity. The total reactivity is 75¢ by switchover with channel 3 contributing 35¢, channel 2 21¢, and channel 4 6¢. Of the 88$/s voiding ramp rate developed by switchover, however, 45$/s comes from channel 3, 12$/s from channel 2 and 22$/s from channel 4.

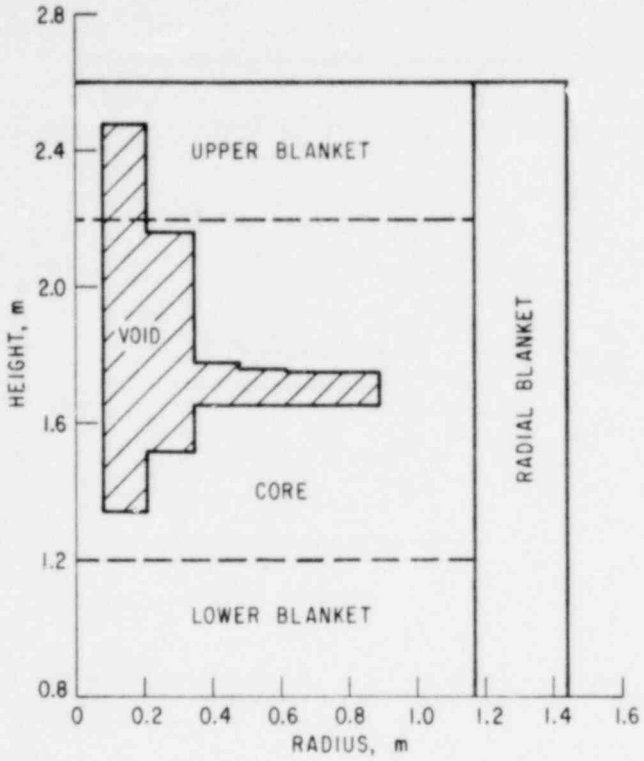

Fig. 21.

Void Pattern at Crossover to Disassembly for 1 $/s TOP WAC Study. ANL Neg. No. 116-79-270.

The net reactivity peaks at about 10 ms FCI time at a value of about 1.18$. The power has not yet peaked at switchover and all channels have failed before switchover except 8. The strong Doppler feedback turns the reactivity around with a negative ramp rate about 2.5 times the amount of the positive sodium ramp at switchover.

Figure 21 shows the extent of voiding of sodium at switchover which was extensive in channels 2 and 3 which have been experiencing FCI for 10.9 and 9.0 ms respectively at crossover. Voiding has hardly begun in the other channels and slug velocities are accordingly far lower.

Results of the Disassembly Phase (Table VIII and Figures 22-24)

The SAS3D/EPIC calculation has not brought the reactor to neutronic shutdown by 3.0 ms after crossover. The calculated normalized power reached a minimum of 163 and began to rise again. About 1.2 ms after crossover, the reactivity fell to a minimum and rose almost to prompt critical again by 3.0 ms disassembly time. While the EPIC calculation of conditions after crossover is not complete, it is felt that the continuation of the calculation leads to unrealistic results.

The present modeling of the disassembly phase in SAS3D/EPIC is inadequate to continue this calculation to neutronic shutdown. Although the conservatism of neglecting radial displacement of fuel inhibits shutdown in the present EPIC model, it is felt at the present time that the more important effect being neglected is the introduction of the very high pressures which result from melting and thermal expansion and the resultant pressurization of fill gas. Presently, the fuel motion causing displacement feedback in EPIC is produced by fuel moving within the pin molten fuel cavity and in the coolant

TABLE VIII. Selected Results from Disassembly Phase for 1$/s TOP WAC Study

Data at Start of Disassembly	Time	s	1.853
	Doppler Constant - core		unavailable
	Doppler Constant - breeder		unavailable
	Net Reactivity	$	1.131
	Ramp Rate (Net-Doppler)	$/s	89
	Peak Fuel Temperature	°C	3330
	Peak Pressure	bar	1.4
	Mass of Molten Fuel	kg	5046
	Fraction of Fuel Molten	%	34
	Normalized Power	-	1806
	Total Energy	MW·s	18963
	Energy of Molten Fuel	MW·s	2410
Results During Disassembly	Duration	ms	3.0
	Max. Fuel Temp.	°C	4372
	Max. (Fuel Vapor) Pressure	bar	20
	Max. Normalized Power	-	2397
	Energy Release	MW·s	5619
	Max. Radial Velocity		not relevant
	Max. Radial Displacement		not relevant
	Max. Axial Velocity		not relevant
	Max. Axial Displacement		not relevant
Results at end of Disassembly	Mass of Molten Fuel	kg	9073
	Fraction of Fuel Molten	%	63
	Mass of Vaporized Fuel	kg	not relevant
	Normalized Power	-	163
	Total Energy	MW·s	24582
	Energy of Molten Fuel	MW·s	5853
Results at end of Isentropic Expansion to 1 bar	Mass of Vap. Fuel	kg	not relevant
	Mechanical Energy	MW·s	125

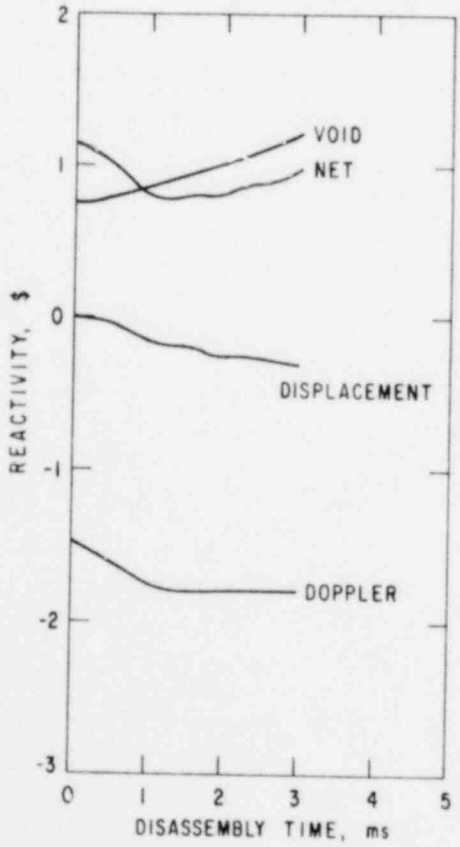

Fig. 22.
Reactivities vs. Disassembly Time for 1 $/s TOP WAC Study. ANL Neg. No. 116-79-290.

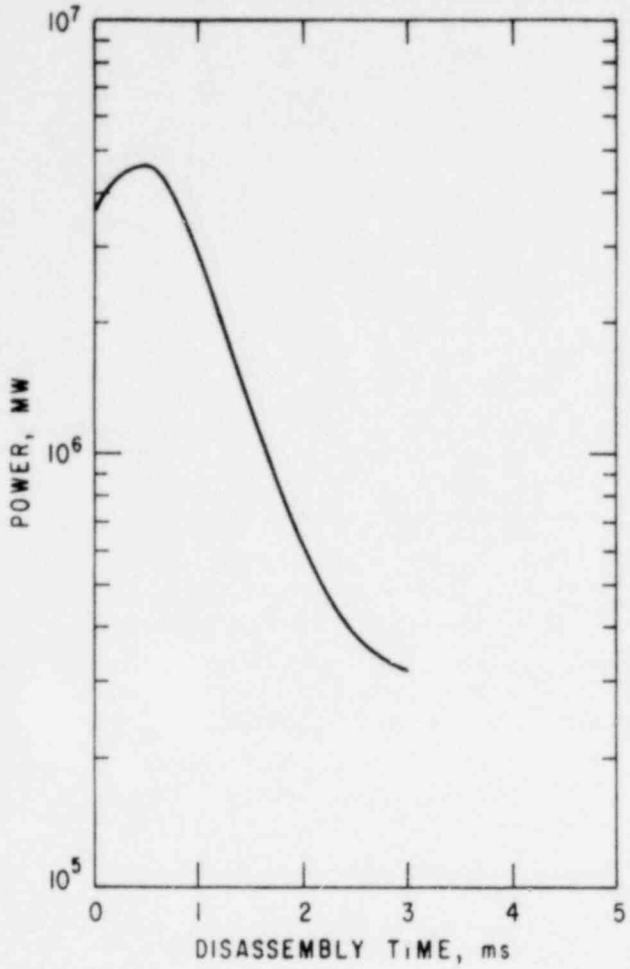

Fig. 23.

Power vs. Disassembly Time for 1 $/s TOP WAC Study. ANL Neg. No. 116-79-285.

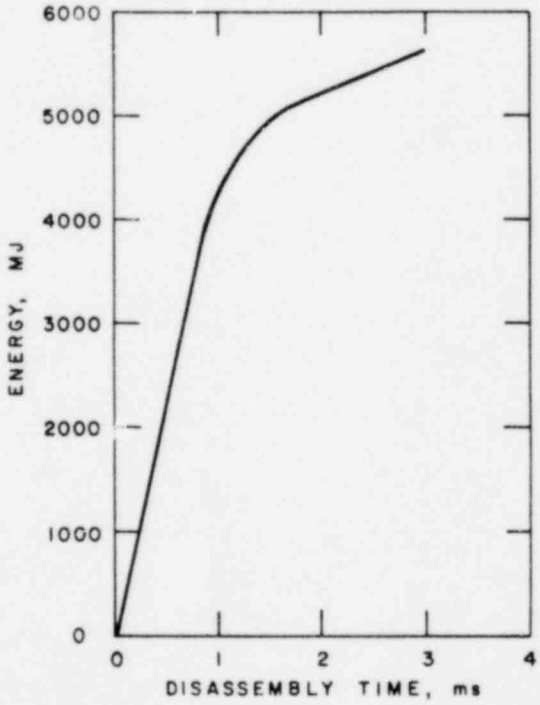

Fig. 24.

Energy vs. Disassembly Time for 1 $/s TOP WAC Study. ANL Neg. No. 116-79-286.

channel. The former is moving under fuel vapor pressure gradients while the fuel in the channel moves under pressure gradients and fuel/sodium drag (almost all the initial shutdown reactivity comes from fuel motion in the channel, however). This fuel is in motion at crossover, which leads to immediate negative feedback. However, the fuel ramp rate (averaged over the first 3 ms of disassembly) is about 100$/s whereas the voiding reactivity is about 150$/s averaged over this time and begins at 88$/s and at 3 ms it is over 200$/s. The displacement feedback is not being produced fast enough to negate the addition of reactivity from sodium voiding and thus the reactivity is increasing.

The maximum fuel vapor pressure attained in the fuel pin is some 20 atm which produced negligible fuel displacement velocities when compared to the single-phase pressures calculated by 2-D disassembly codes such as VENUS or KADIS. There is significant feedback resulting from the motion of the channel fuel which is moving far faster than the pin fuel but there is only 12 g per pin in the channel which limits its effect in the longer run.

In spite of the fact that the reactor is not shut down, a summary of results is provided including molten fuel data, total energy and work energy potential computed at the time the calculation was cut off. However, these data represent a different physical situation than that of corresponding numbers of the other codes

2. Results for the WAC 10¢/s TOP Irradiated Core Exercise
(P. A. Pizzica and H. H. Hummel)

The present calculations start with the steady-state initialization (as calculated at KfK using SAS3D) after 275 days of operation and proceed to 100 ms past initial fuel-pin failure. In this SAS3D/EPIC calculation, no axial averaging of fission gas pressure was calculated. The gas released at each axial node was assumed to pressurize the node at that axial location and this hoop stress was compared to the clad strength at that node. (The two cases listed below were also run averaging the fission gas pressure over the length of the molten cavity with no change in failure location and no essential change in results.)

In order to decide how the pin fails according to this burst pressure criterion, it seems necessary to consider more than the hoop stress loading the clad in some fashion and the strength of the clad at the point where the gas pressure is assumed to load it. It is also necessary to consider the constraint that the solid fuel annulus provides on the escape of fission gas and of molten fuel from the center of the pin. If the fuel melt fraction is too low, it seems unrealistic to assume that molten fuel can be ejected into the coolant channel since the annulus could be assumed to contain the molten fuel and it would be more difficult to have interconnected cracks in the fuel leading to the clad breach and it is also possible for molten fuel to freeze in the cracks, at least prior to failure, thus plugging escape routes.

It was therefore decided to require a certain minimum fuel melt fraction at the node where failure would be predicted according to a fission gas loading criterion. Two values for this minimum were used: 0.4 and 0.6. Values below 0.4 could be expected to produce conditions after pin failure

similar to the 0.4 case since the failure would be higher up in the core. A melt fraction greater than 0.6 certainly seems unnecessary for burst failure conditions.

Table IX shows pin conditions up to failure time. Since an indication of the events following pin failure might be helpful in choosing a pin failure criterion, the two calculations were continued until about 100 ms after first pin failure. In the first case with 0.4 minimum fuel melt fraction, although there was some positive feedback from coolant voiding, the negative feedback of fuel motion upwards from (and, in the pin, to) the clad rip (which occurs at 80% of core height) at first equals and then exceeds the voiding feedback, and by 100 ms after failure, there is -1.17$ from fuel motion, 0.58$ from coolant (of which 0.44$ is from channel 2) and the reactor power has declined to 1.7 from 3.5 at pin failure. Net reactivity is -0.40$. No additional channels failed by this time.

The case with the 0.6 minimum is somewhat more interesting. The first failure occurs in channel 2 at 60% of core height. An excess of positive feedback from voding and fuel motion exceeds the negative feedback from fuel motion to bring the reactor power up to about 30 times nominal from 3.7 at pin failure, before the negative ramp from fuel motion becomes more important than that from the coolant. The power declines to about 3.0 when pin failure occurs in channel 4 at node 10. This is 44 ms after first pin failure. There is another mild power rise to about 10 times nominal and again fuel motion brings it down to about 4.0 when pin failure occurs in channel 6 at node 10 (68 ms after first pin failure). The power rises to about 6.0 times nominal and then declines to about 1.7 at about 91 ms after first pin failure. Net reactivity is -0.62$. At this time, channel 1, the highest power fresh fuel channel, has a maximum of 0.7 fuel melt fraction with an average fuel temperature of 3556 K (maximum fuel temperature of 4886 K giving approximately 30 atm vapor pressure). Pin failure would probably not be predicted in any fresh fuel channels.

Fuel pin failure criteria and post-failure modeling will be discussed at the next meeting of the WAC group.

3. Analysis of PBE-5S (P. L. Garner, P. B. Abramson, and B. A. Greer)

A previous report[32] presented a model for describing autoclave hydrodynamics and illustrated the effects of modeling assumptions upon pressure wave propagation calculations. A series of calculations has been performed to investigate the range of source pressurizations which are consistent with the pressures measured during the PBE-5S experiment.[33] All calculations assumed a source pressure at the failure location which decayed from pressure P_o to 0.1 MPa over time t_c; the piston motion delay time, t_p, and location of the top of the initial failure zone, Z_t, were also varied. Pressures at the top of the autoclave and the piston motions calculated for several cases are shown in Fig. 25. All four of the calculated pressure histories are in good agreement with the pressure measured during the test in spite of significant variations in characterization of the source (P_o varying by 30%, t_c from 1.8 to 2.2 ms, t_p from 0 to 0.3 ms, and Z_t by 100 mm). Although the calculated piston motions as shown are in poor agreement with the experiment, the agreement would be improved substantially if the motion history from the experiment were to be shifted back in time by 0.5 to 0.75 ms (reflecting a possible synchronization error between pressure and piston motion data from the experiment). The

TABLE IX. Channel 2 Pin Characteristics up to Failure for 10¢/s TOP WAC Study

Time[a] (s)	Clad Hoop Stress (dynes/cm^2)	Clad Failure Stress (dynes/cm^2)	Clad Temp. (K)	Avg. Fuel Temp. (K)	Fission Gas Press. (dynes/cm^2)	Fuel Melt[b] Fraction	Release Frac.[c] Radially Avg.
		Case 1: 0.4 Minimum Fuel Melt Fraction at Failure Node (13)					
0.200	$1.402 \cdot 10^8$	$4.482 \cdot 10^9$	865	1708	$2.336 \cdot 10^7$	-	0.0003
2.200	$1.512 \cdot 10^8$	$4.278 \cdot 10^9$	880	1776	$2.489 \cdot 10^7$	-	0.014
3.514	$1.614 \cdot 10^8$	$4.014 \cdot 10^9$	898	1867	$2.631 \cdot 10^7$	-	0.023
5.066	$1.760 \cdot 10^8$	$3.639 \cdot 10^9$	925	2000	$2.834 \cdot 10^7$	-	0.033
6.801	$1.984 \cdot 10^8$	$3.148 \cdot 10^9$	961	2172	$3.146 \cdot 10^7$	-	0.049
8.391	$2.613 \cdot 10^8$	$2.620 \cdot 10^9$	1002	2348	$4.019 \cdot 10^7$	-	0.104
9.491	$3.569 \cdot 10^8$	$2.234 \cdot 10^9$	1035	2472	$5.346 \cdot 10^7$	0.037	0.182
10.446	$4.986 \cdot 10^8$	$1.898 \cdot 10^9$	1066	2563	$7.313 \cdot 10^7$	0.136	0.276
11.384	$7.018 \cdot 10^8$	$1.591 \cdot 10^9$	1098	2667	$10.13 \cdot 10^7$	0.248	0.378
12.192	$9. \cdot 10^8$	$1.320 \cdot 10^9$	1129	2781	$13.58 \cdot 10^7$	0.338	0.473
12.776	$11 \cdot 10^8$	$1.126 \cdot 10^9$	1155	2893	$16.59 \cdot 10^7$	0.405	0.528
		Case 2: 0.6 Minimum Fuel Melt Fraction at Failure Node (11)					
0.200	$1.360 \cdot 10^8$	$4.912 \cdot 10^9$	834	1850	$2.336 \cdot 10^7$	-	0.0004
2.200	$1.479 \cdot 10^8$	$4.734 \cdot 10^9$	847	1926	$2.501 \cdot 10^7$	-	0.017
3.514	$1.613 \cdot 10^8$	$4.512 \cdot 10^9$	863	2027	$2.688 \cdot 10^7$	-	0.032
5.066	$1.702 \cdot 10^8$	$4.191 \cdot 10^9$	886	2172	$2.812 \cdot 10^7$	-	0.035
6.801	$1.947 \cdot 10^8$	$3.762 \cdot 10^9$	916	2352	$3.153 \cdot 10^7$	-	0.055
8.391	$2.693 \cdot 10^8$	$3.292 \cdot 10^9$	951	2497	$4.188 \cdot 10^7$	0.089	0.123
9.491	$3.737 \cdot 10^8$	$2.953 \cdot 10^9$	976	2601	$5.637 \cdot 10^7$	0.202	0.199
10.446	$5.234 \cdot 10^8$	$2.635 \cdot 10^9$	1001	2720	$7.715 \cdot 10^7$	0.313	0.282
11.384	$7.752 \cdot 10^8$	$2.303 \cdot 10^9$	1029	2873	$11.21 \cdot 10^7$	0.415	0.386
12.192	$11.39 \cdot 10^8$	$1.982 \cdot 10^9$	1058	3027	$16.26 \cdot 10^7$	0.498	0.499
13.045	$16.02 \cdot 10^8$	$1.628 \cdot 10^9$	1094	3215	$22.68 \cdot 10^7$	0.557	0.591
13.395	$18.98 \cdot 10^8$	$1.473 \cdot 10^9$	1111	3299	$26.79 \cdot 10^7$	0.601	0.630

[a]Last times in column are times of pin failure.

[b]Maximum fuel melt fraction for Case 1 at pin Failure was 0.555, for Case 2, 0.615.

[c]This is the fraction of steady-state retained gas released averaged over the unrestructured nodes.

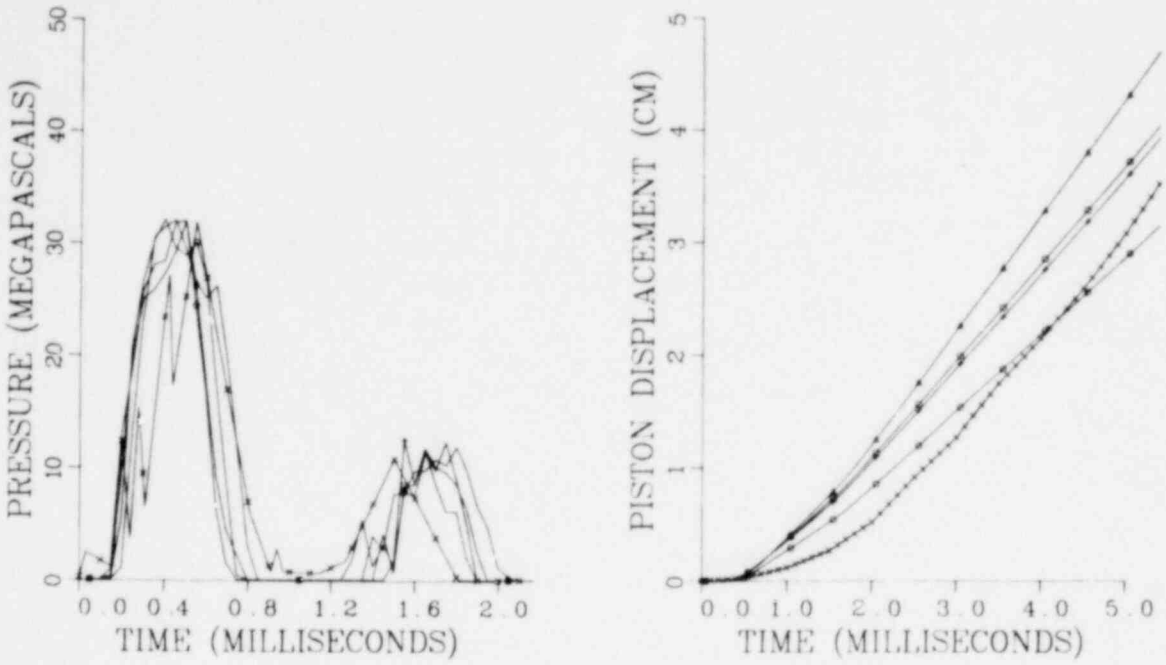

Fig. 25. Pressure below piston (a) and piston motion (b) calculated for various source pressures and modeling assumptions.

- P_o = 30 MPa, t_c = 1.8 ms, t_p = 0.24 ms, $Z_t = Z_{to}$
o - P_o = 23.5 MPa, t_c = 1.8 ms, t_p = 0.3 ms, $Z_t = Z_{to}$+50 mm
Δ - P_o = 41.6 MPa, t_c = 2.2 ms, t_p = 0.2 ms, $Z_t = Z_{to}$-50 mm
\+ - P_o = 26 MPa, t_c = 1.8 ms, t_p = 0 ms, $Z_t = Z_{to}$ + 38 mm
× - PBE-5S experiment
ANL Neg. No. 116-79-192R1

calculations are a companion to those presented in Ref. 34 which showed that a wide range of source pressure characterizations (as induced by variations in EPIC parameters) could give similar piston motion histories.

The compressible hydrodynamics treatment of the sodium slugs has been incorporated into a version of the EPIC code. Results of a typical calculation are shown in Figs. 26 and 27. Calculational conditions are the same as those used for Curve 1 of Fig. 10 in Ref. 34 but increase the coefficients for heat transfer from fuel and sodium to the structure by a factor of 10 and include a 0.25 ms piston-motion delay time. The calculated piston motion is in excellent agreement with that measured during that experiment. There is little similarity between the calculated and measured pressures; this is not totally surprising since there seems to be an inconsistency in the experiment data (cf. discussion related to Fig. 4 of Ref. 32 and Fig. 1 of Ref. 35). The only point of agreement is the period between pulses at the bottom of the autoclave, although the calculated values are displaced in time by half a period from the experiment values. The lack of agreement is also affected by the degree to which the autoclave can be properly represented by the 1-D EPIC code using constant mesh spacing (25mm in this case). The general discrepancy in magnitude of the first peak is compounded by uncertainties in pin failure conditions, fuel-to-coolant heat transfer modeling uncertainties, and uncertainties in thermophysical properties (e.g., fuel vapor pressure). Indeed, the magnitude of the measured pressure peaks can be

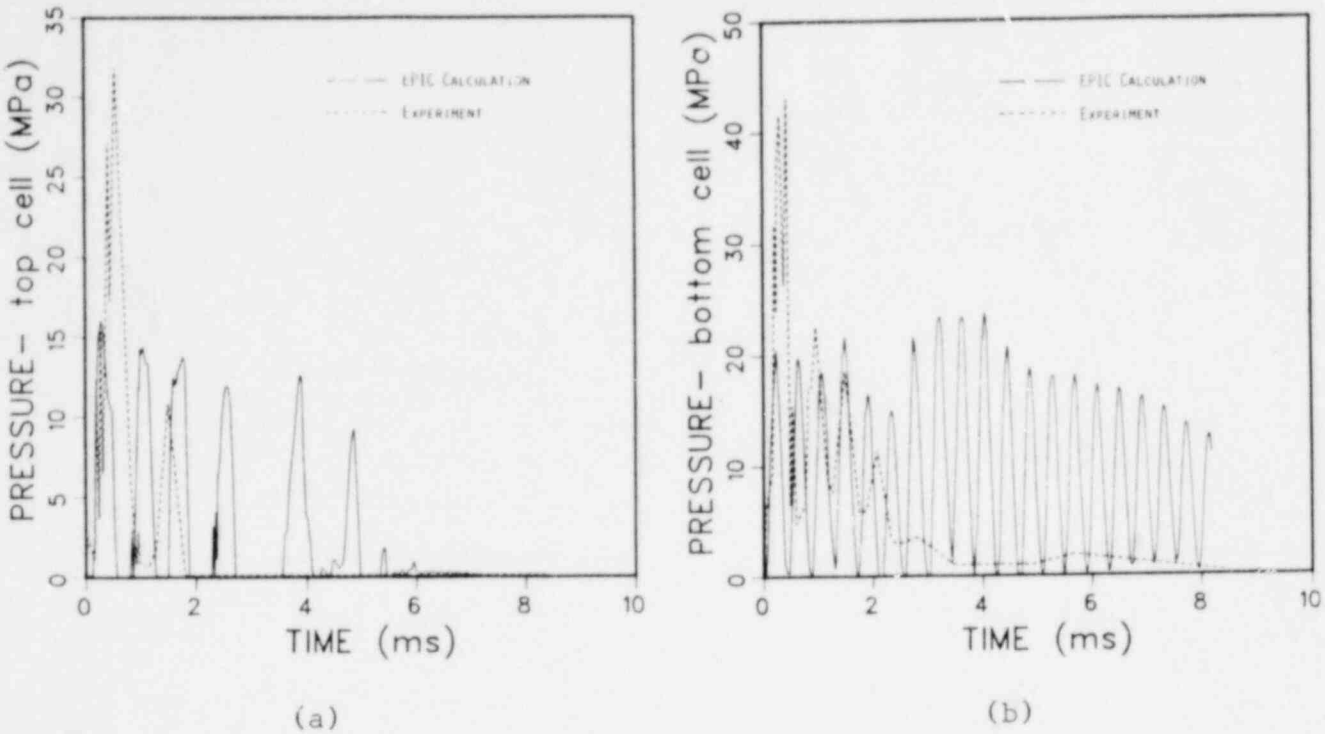

Fig. 26. Pressure below piston (a) and pressure at bottome of autoclave (b) for PBE-5S.

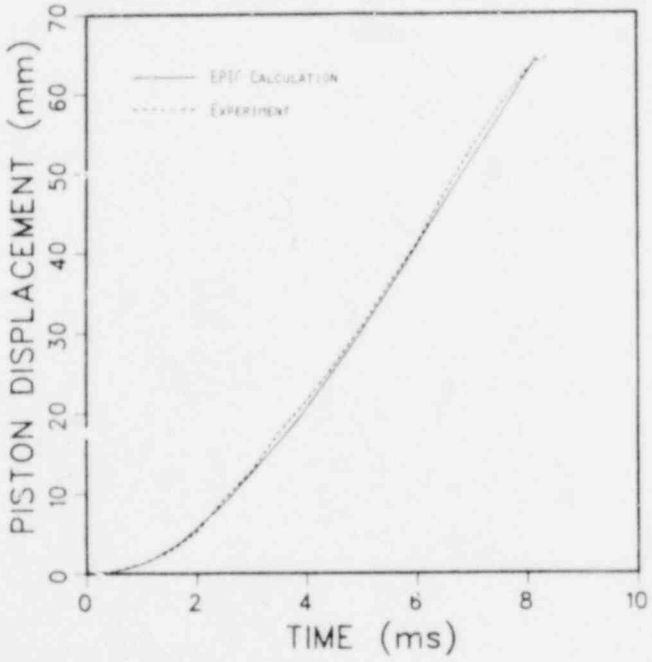

Fig. 27.

Piston motion history for PBE-5S.

matched by postulating an increase in the fuel vapor pressure data by a factor of two (which is well within the data uncertainties).

Discussions have been held with personnel at Sandia Laboratories to try to resolve data and piston motion uncertainties. The implementation of the compressible treatment needs to be modified to use a timestep subdivision logic to shorten the computation time, since the timestep is now dictated by sound, rather than material, speed considerations.

4. Consultations

P. B. Abramson and P. L. Garner visited Sandia Laboratories on April 9 to discuss analysis of PBE tests with W. Camp and M. Young. In addition, discussion covered data availability, error bounds, data reduction techniques and potential inconsistencies. W. Camp will check the question of synchronization of piston displacement and pressure traces from PBE-5S and provide us with estimates of maximum error bounds.

P. L. Garner attended the ASME workshop and symposium on Multi-Phase Flow and Heat Transfer from April 16-18.

M. F. Kennedy visited BNL on April 30 to discuss Loss of Heat Sink with R. Bari, T. Pratt and K. Perkins. In addition he held brief discussions with T. Ginsberg and G. Greene on the hydrodynamics experiments.

J. J. Sienicki and P. B. Abramson attended the ANS M&C topical at Williamsburg, VA, where they presented an invited paper on the TWOPOOL methodologies for solution of combined compressible and incompressible two-phase flows.

P. L. Garner attended the WAC meeting in Brussels on May 15 and then visited laboratories at Karlsruhe (May 17-18), Cadarache (May 21-22), Grenoble (May 23) and Ispra (May 28-June 1) for technical discussions related to boiling and voiding and to EPIC development and use in analyzing experiments.

II. MONTE CARLO ANALYSIS AND CRITICAL PROGRAM PLANNING FOR SAFETY-RELATED CRITICALS

(A2018)

A. Monte Carlo Analysis of Safety-Related Criticals (L. G. LeSage and E. M. Gelbard)

Reexamination of Monte Carlo output for the RSR criticals experiments has revealed significant internal discrepancies among various VIM estimators. It has been determined that these discrepencies were due to an error in an input preparation routine specially written to compile VIM input decks for very detailed simulations. This error has been corrected, and Monte Carlo computations for the RSR criticals sequence have been rerun. Revised VIM eigenvalues are listed in Table X. Results labelled 1, 3 and 4, each based on 100,000 histories, have already been reported in Ref. 2. Since completion of the Ref. 2 calculations the Monte Carlo analysis of case 2 has been somewhat refined, and results of the more recent case 2 calculations have been included in Table X. The case 2 eigenvalue which appears in Table X is an average over three separate runs, of 100,000 histories each. Data from these separate and independent runs are displayed in Table XI.

Table X. Best Estimates

Case #	λ	C/E
1 (Reference Core)	0.996 ± 0.002	0.995 ± 0.002
2 (Na Voided Reference Core)	0.993 ± 0.001	0.996 ± 0.001
3 (Slump Out)	0.996 ± 0.002	0.996 ± 0.002
4 (Slump In)	1.001 ± 0.002	1.000 ± 0.002

Table XI. Eigenvalue for the Sodium-Voided Configuration

	λ	
Run 1	0.9884 ± 0.0024	Run with original deck
Run 2	0.9957 ± 0.0025	
Mean	0.9920 ± 0.0017	
Run 3	0.9960 ± 0.0020	Run with deck generated from Ref. Core deck

Run 1 and 2, referred to in Table XI, were both started from the same source guess, and were run with the same input deck, but with different starting random numbers. The case 2 eigenvalue which appears in Ref. 2 was taken from run 1.

The input deck used for runs 1 and 2 was compiled directly from loading diagrams for the sodium-voided RSR configuration. On the other hand input for run 3 was constructed from the case 1 (Reference Core) input deck, by withdrawing sodium from some of the coolant channels. This change in the case 1 input deck was accomplished manually, without recourse to any automation. The run 1, run 2 and run 3 configurations should be identical, aside for small random differences in number densities of nominal ℓ_y identical plates, and except for the presence, in run 3 of uranium foils. These foils were originally modeled in the input for the Reference Core and were allowed to remain in the run 3 core, though there were really no such foils in the sodium-voided critical configuration. Because of the presense of the foils the run 3 deck is entirely different from the original input deck used for run 1 and 2, although the foils should be too thin to generate substantial perturbations. Since the deck for run 3, and the deck used for runs 1 and 2, were constructed by such different processes, intercomparisons between them should help to validate automated methods used to prepare VIM input for the RSR sequence.

The mean, $\lambda_{(1,2)}$, of VIM eigenvalues for runs 1 and 2, is 0.9920 ± 0.0017: $\lambda_{(3)}$, the VIM eigenvalues for run 3, is 0.9960 ± 0.0020. Thus $\lambda_{(3)} - \lambda_{(1,2)} = 0.004 < 0.003$, so that he difference between these eigenvalues is somewhat greater than a standard deviation. There is here, however, no indication of a real discrepancy. It will be seen that the difference between run 1 and run 2 eigenvalues is surprisingly large but this difference, also, seems at present to be statistical.

Of course the reasonably good agreement between the eigenvalues $\lambda_{(3)}$ and $\lambda_{(1,2)}$ does not, in itself, prove that the two sodium-voided input decks are identical. But, in order to validate the input preparatin codes used to write VIM input for the RSR configurations (codes which may be generally useful for work on other critical configurations), it is important to pinpoint any differences between these decks. Therefore they have been, and will be, very carefully compared.

Net inventories of sodium, uranium and plutonium, compiled from data in both decks and computed from VIM edits, are shown in Table XII. These inventories, generally, agree very well with each other, except for an 11 gram discrepancy in sodium content. It has been established that this discrepancy is due to random differences in the mean density of sodium in different sodium plates.

Further tests on these same decks will soon be carried out. In the course of these tests points will be selected from a uniform distribution over a region containing the whole reactor configuration. Using geometry routines in VIM, and one of the input decks, a composition will be assigned to each point. Then, using the other deck, a second composition will be assigned to each point. Finally, at each point, the two conpositions will be compared

and any differences will be noted. The utility of the proposed procedure will depend on its efficiency, and connot yet be assessed.

Table XII. Net Inventories in Sodium-Voided Configuration Input Decks

Nuclide	Mass (gms)	
	Original Deck	Sodium-Voided Ref. Core Deck
Na	15,998.9	16,010.2
^{235}U	118.61	118.62
^{238}U	55,337.8	55,336.0
^{239}Pu	415.22	415.22

Masses listed here are taken directly from VIM edits.

Three-Dimensional Code Development for Core Thermal-Hydraulic Analysis of LMFBR Accidents under Natural Convection Conditions

(A2045)

A. Summary (W. T. Sha)

The objective of this program is to develop computer programs (COMMIX and BODYFIT) which can be used for either single-phase or two-phase thermal-hydraulic analysis of reactor components under normal and off-normal operating conditions. The governing equations of conservation of mass, momentum and energy are solved as a boundary value problem in space and initial value problem in time.

COMMIX is a three-dimensional, transient, compressible flow component computer code for reactor thermal-hydraulic analysis using a porous medium formulation. The concept of volume porosity, surface permeability, and distributed resistance and heat source (or sink) is employed in the COMMIX Code for quasi-continuum (or rod-bundle) thermal-hydraulic analysis. It provides a greater range of applicability and an improved accuracy than subchannel analysis. By setting volume porosity and surface permeability equal to unity, and resistance equal to zero, the COMMIX Code can equally handle continuum problems (reactor inlet or outlet plenum, etc.).

BODYFIT is a three-dimensional, transient, compressible flow component computer code for reactor rod bundle thermal-hydraulic analysis using a boundary-fitted coordinate transformations. The complex rod bundle geometry is transformed into either rectangular or cylindrical coordinates with uniform mesh. Thus, the physical boundaries, including each rod, coincide with computational grids. This allows the numerical solution of the Navier-Stokes equations, together with the boundary conditions to be represented accurately in the finite-difference formulation. Thus, the region in the immediate vicinity of solid surfaces, which is generally dominant in determining the character of the flow, can be accurately resolved.

B. COMMIX-1, Single Phase Code Development (H. M. Domanus)

1. Thermal Modeling of Solid Structures (H. M. Domanus and M. J. Chen)

To analyze the thermal-hydraulic characteristics of the coolant (sodium) in an LMFBR fuel assembly undergoing a transient, the solid structures in contact with the coolant must be considered. Thermal models of the fuel, clad, wire wrap spacers, filler wires and duct walls have been formulated and implemented into COMMIX-1A. These initial models are somewhat restrictive in their scope of possible application. To relieve some of these limitations, code restructuring appears necessary.

This restructuring is aimed at a more general treatment of thermal interaction between the coolant (sodium) and adjacent solid structures. It has been implemented as an option so that the original fuel rod modeling could be used for applicable cases to reduce input requirements. Before the new

thermal structures model can replace the original fuel rod model, specific subroutines should be written to reduce the input required for the treatment of helical wire wrap spacers and gamma heating.

2. One-Equation Turbulence Model (M. J. Chen and H. M. Domanus)

The one-equation turbulence model has been implemented into COMMIX-1A. Preliminary comparisons of the steady state 7-pin with and without the one-equation turbulence model show small differences in the velocity and temperature fields. Further investigations with different operating conditions are underway.

3. W-1 Pretest Simulation (H. M. Domanus and M. J. Chen)

A pretest analysis of the W-1 loss of piping integrity transient experiment was performed using COMMIX-1A. The results were compiled and documented. As the W-1 experimental measurements become available, the post-test analysis will begin.

4. 7-Pin Flow Rundown Transient[36] (H. M. Domanus and M. J. Chen)

To evaluate the adequacy of existing models and establish the need for new models, analysis of the German 7-pin flow rundown experiments has served as our basis. Many parametric studies have been performed and compared to both the steady-state and transient experimental results. From these studies the "recommended" values of both operating and physical modeling parameters are being improved.

5. Drag Force Modeling (H. M. Domanus)

To better model the pressure drop of the rod bundle, a drag force structure has been formulated and implemented into COMMIX-1A. This new force structure allows the user to impose a specific force $\overline{F}$ in terms of three components F_x, F_y, and F_z at any location in the flow field, where for example, $F_z = -\alpha\,(\phi/L)\rho w\langle w\rangle$, F_x and F_y are similarly defined.

Here the specific force component F_z is directed in the positive z-direction and has the units (nt/m^3) where

α = volume porosity (dimensionless)

ρ = density (Kg/m^3)

w = velocity in z-direction (m/sec)

L = characteristic length (m), and

ϕ = drag correlation (dimensionless) having the form

$$a_\ell Re^{b_\ell} + C_\ell \qquad Re \leq Re_{tr}$$

$$a_t Re^{b_t} + C_t \qquad Re \leq Re_{tr}$$

Re = Reynolds number (dimensionless).

In the process of implementing the force structure model and applying it to the grid spacers in the 7-pin configuration, an anomaly in the pressure distribution was detected. As the flow goes past a grid spacer, there is flow area contraction, then an expansion. The pressure recovery after the expansion was found to be shifted one computational cell downstream from where expected. While examining the finite difference equations, a new representation for the convective terms of the momentum equations was formulated. This new formulation has been implemented into COMMIX-1A and has eliminated the pressure shift.

6. Computational Techniques (H. M. Domanus)

In an effort to speed up the steady-state and transient calculation, a mass rebalancing option has been formulated and implemented into COMMIX-1A. This first rebalancing option is rather specific in that it is applied only in the z-direction, where the inlet is adjacent to the K = 1 plane, and the exit at the K = KMAX plane. This is the case for all hexagonal fuel assembly smulations studied up to the present time. The first application of this mass rebalancing option was to the Germ..n 7-pin flow rundown transient. With all other parameters the same, a comparison between the running times with and without the rebalancing indcates the rebalancing to be three (3) times faster. In addition, the global conservation of mass and energy are also improved, thus implying a higher quality solution.

A transient pressure boundary condition has also been implemented into COMMIX-1A. The new boundary condition is necessary when both the inlet flow and inlet pressure are specified, as in the W-1 pretest analysis.

C. COMMIX-2, Two-Phase Code Development (V. L. Shah, J. L. Krazinski, C. C. Miao, G. Leaf, S. M. Prastein, and W. T. Sha)

1. General Remarks

In order to improve the convergence rate of the cell-by-cell iterative procedure, a block iterative solution method was investigated. The block iterative technique is expected to have a faster rate of convergence, being more implicit than the cell-by-cell procedure. The block iterative method required reformulation of the conservation equations, such that all the conservation equations possessed a common form. In addition, code modifications were needed in order to implement the Fast Fourier Transform technique.

2. Accomplishments

The finite difference formulations for the block iterative solution technique have been implemented in the code. Simple problems were run to debug and test the solution scheme. Debugging options, which can be selectively turned on, were incorporated in all pertinent subroutines to aid in this task. Single-phase (liquid) flow problems were being run during this initial period to debug and evluate the block iterative solution scheme.

The modifications necessary for the Fast Fourier Transform procedure have been completed. After the new section of coding was debugged, sample problems were run to evaluate this technique. Two single-phase-flow problems were run using the Fast Fourier Transform procedure: a three-dimensional, isothermal duct flow and a three-dimensional, non-isothermal problem. These preliminary results indicate significant potential improvements over the running times obtained with the cell-by-cell iterative procedure.

D. BODYFIT-1, Single-Phase Code Development (B. C-J. Chen, W. T. Sha)

Several major modifications had been implemented in BODY-FIT to improve the accuracy of the calculation and the rate of convergence. The most significant ones are listed as follows:

1. A new coordinate system was generated. It has a branch cut from the center fuel pin to the outside duct wall as shown by the dash line in Fig. 28. It transforms the hex geometry in one piece instead of three pieces used in the previous coordinate transformation. The coordinate lines are much more orthogonal, the symmetry is better preserved, and the interconnection between different regions of the hex are much stronger in this new transformation.

2. A pointer system for numbering the computational cell was devised to save computer storage space. It eliminates the storage space used previously for all the interior points of the fuel pin. It results in approximately 30% saving in core storage space.

3. Several options were added in the code to extend the capabilities of the code. It can calculate a one-twelfth sector of the hex fuel assembly. It is applicable to square geometry, hex geometry, or cylindrical geometry. It can skip calculations for momentum equation or energy equation or both.

4. The plane-by-plane mass rebalance technique was incorporated in the code. It improves the rate of convergence by factors of 3 to 10, depending on the geometry.

5. A new subroutine was written to improve the calculational accuracy and the rate of convergence in the stress terms of the momentum equation. It eliminated all the cross second derivatives in computing the stress terms.

In order to establish the confidence of this procedure, two sample problems were analyzed; i.e., rectangular ducts and two concentric rings with variable aspect ratios. The configurations before and after the boundary-fitted coordinate transformation are given in Fig. 29 and Fig. 30 for the rectangular duct and the concentric rings, respectively. The code predicted value versus analytical results[37] for the center line velocity of the rectangular ducts of various aspect ratios are given in Fig. 31. The code predicted versus the analytical[38] axial velocity profile and the center line velocity of the concentric rings are given in Fig. 32a and 32b, respectively. The agreements between the code predictions and the analytical results are excellent.

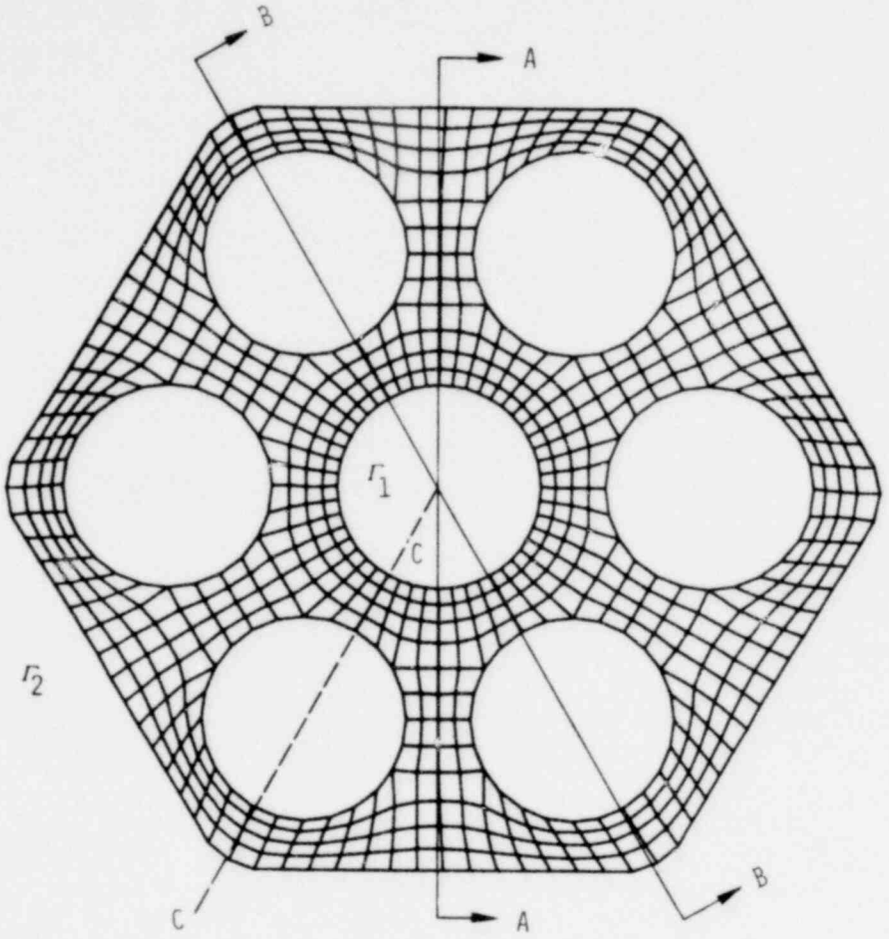

RADIUS = 3.0 MM
GAP BETWEEN PINS = 1.9 MM
FLAT TO FLAT = 22 MM
V_M = 2.15 M/S
RE = 3.373×10^4
HEAT FLUX = $.993 \times 10^6$ WATTS/M^2

(a)

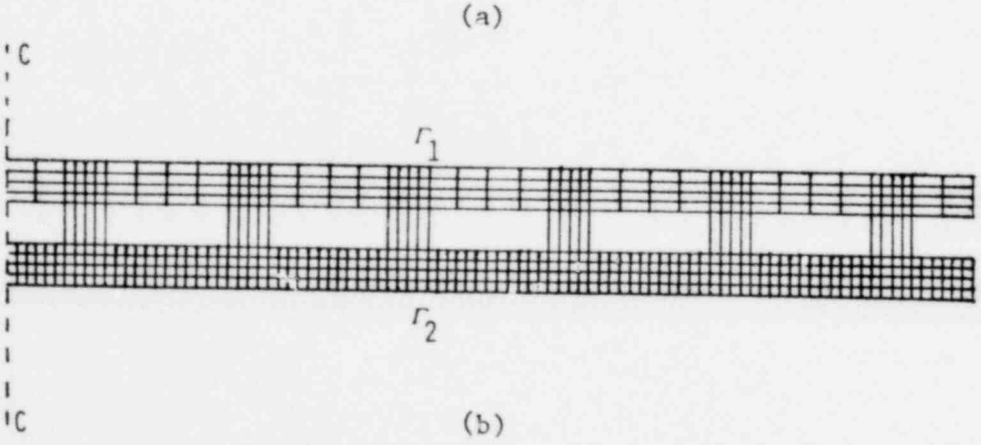

(b)

Fig. 28. (a) Physical Dimensions and Coordinates
(b) Transformed Coordinates
ANL Neg. No. 116-79-192R1

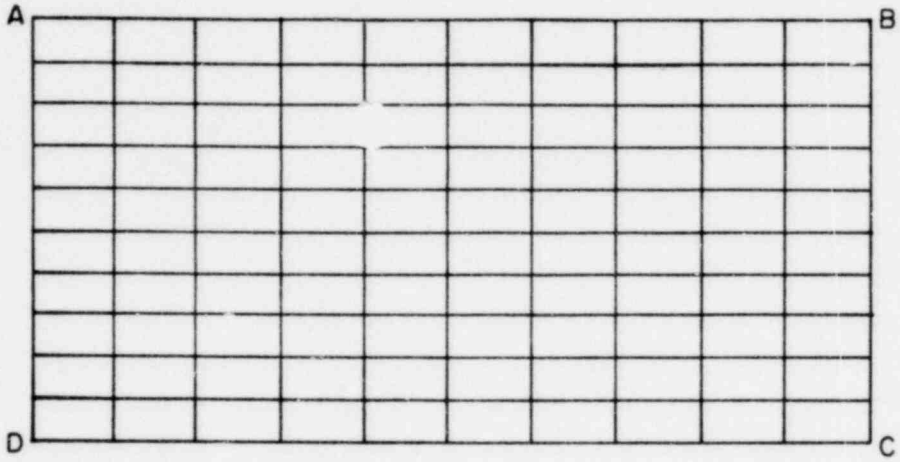

Fig. 29a. Coordinate Lines for the Rectangular Duct before the Transformation. ANL Neg. No. 116-79-283.

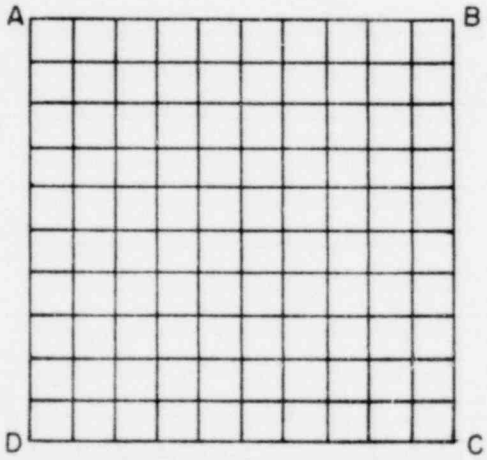

Fig. 29b.

Coordinate Lines for the Rectangular Duct after the Transformation. ANL Neg. No. 116-79-283.

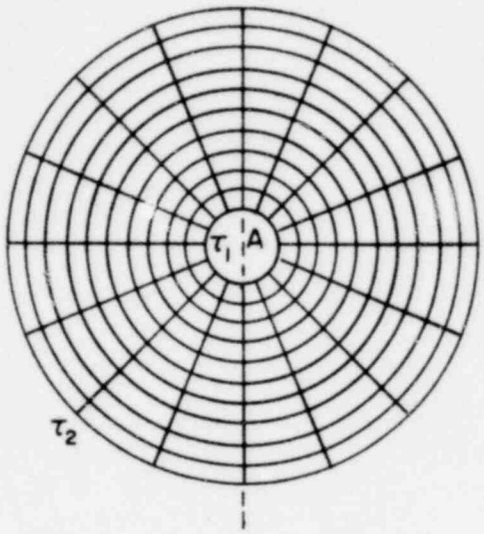

Fig. 30a. Coordinate Lines for the Concentric Ring before the Transformation. ANL Neg. No. 116-79-282.

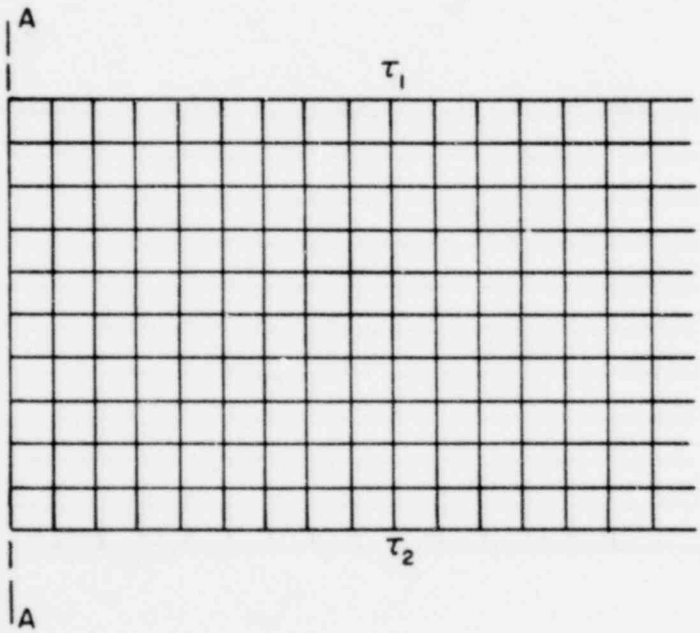

Fig. 30b. Coordinate Lines for the Concentric Ring after the Transformation. ANL Neg. No. 116-79-282.

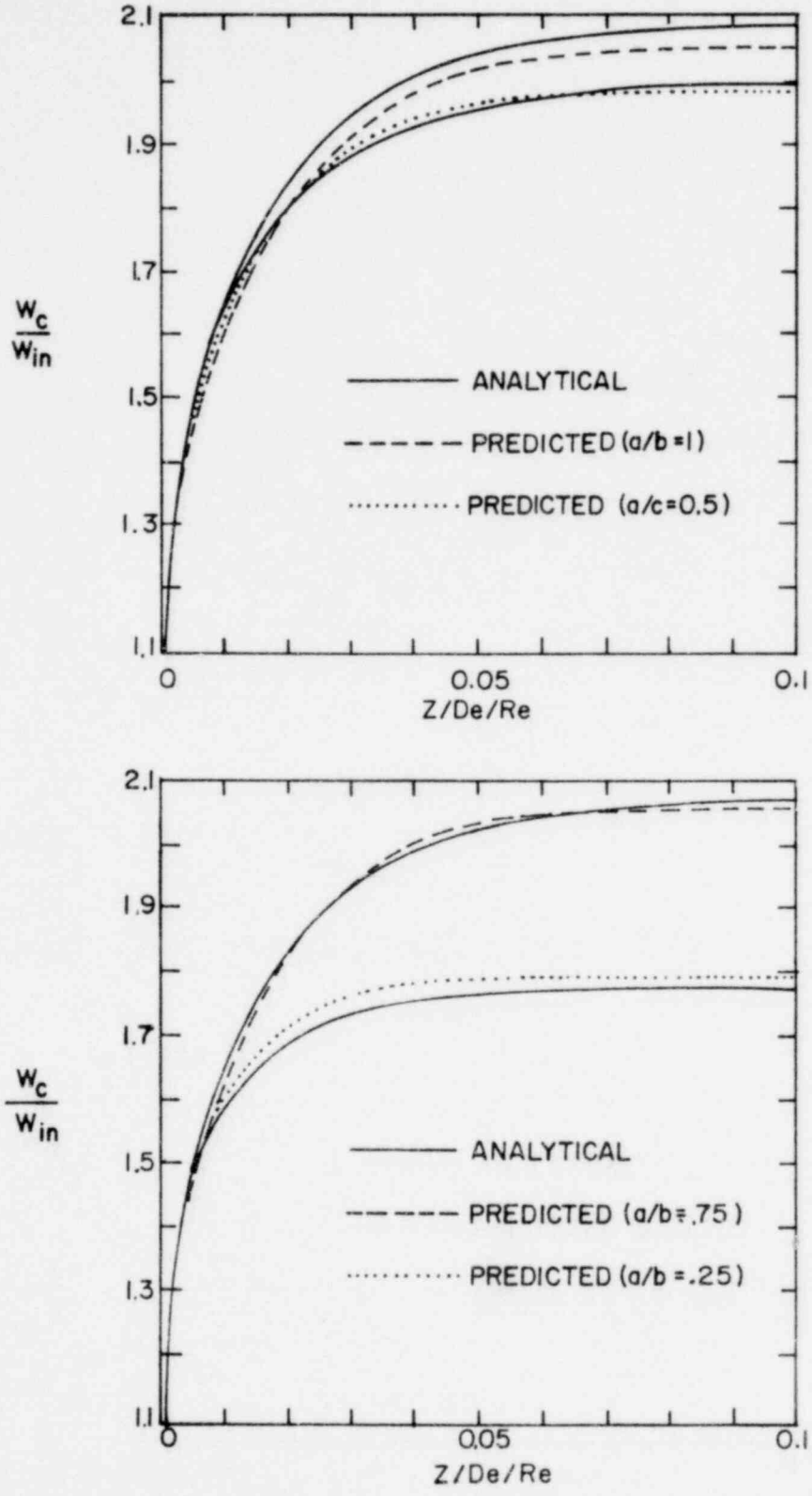

Fig. 31. The Center Line Velocity for Rectangular Ducts of Various Aspect Ratios. ANL Neg. No. 116-79-280.

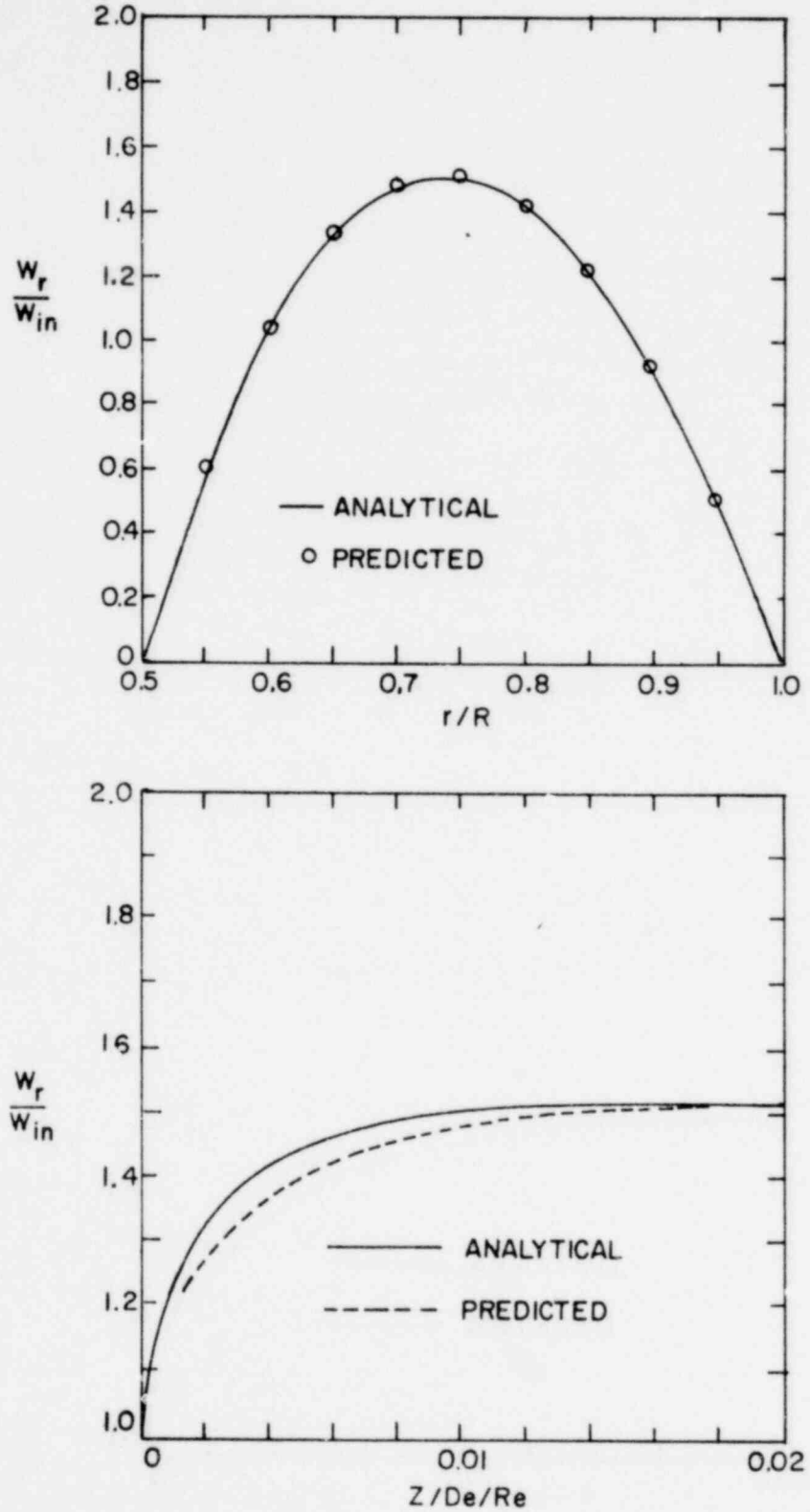

Fig. 32. The Radial Velocity and the Center Line Velocity for the Concentric Rings with the Aspect Ratios of 0.5. ANL Neg. No. 116-79-281.

Simulation of a 7-pin hex fuel assembly was also performed to compare with the experimental measurements.[36] The comparison between measurements and predictions are given in Fig. 33. Reasonable agreements are achieved.

Modeling of the spacer grids and the fuel pin model are currently under way to improve the predicted values. The inclusion of the thick duct wall will also be considered in the simulation.

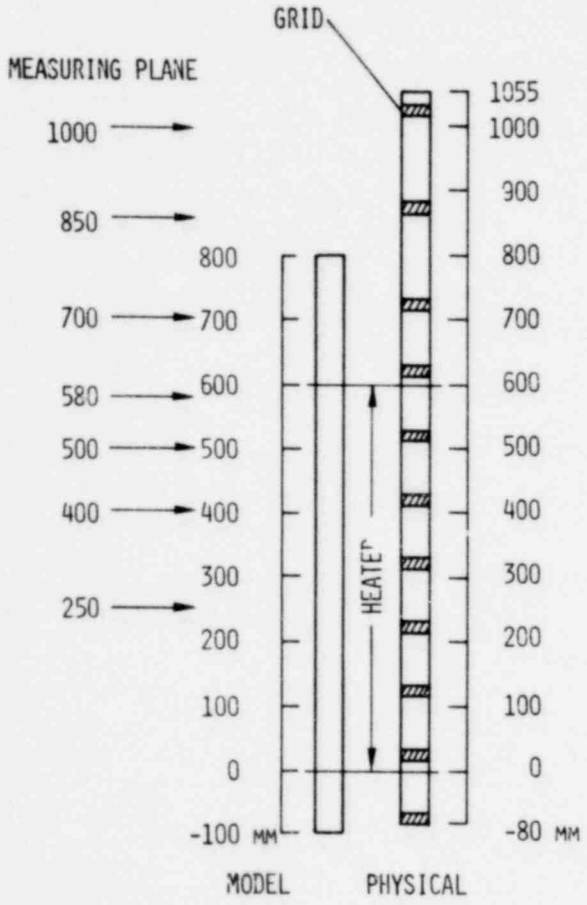

Fig. 33a.

Physical Modeling. ANL Neg. No. 116-79-191R1.

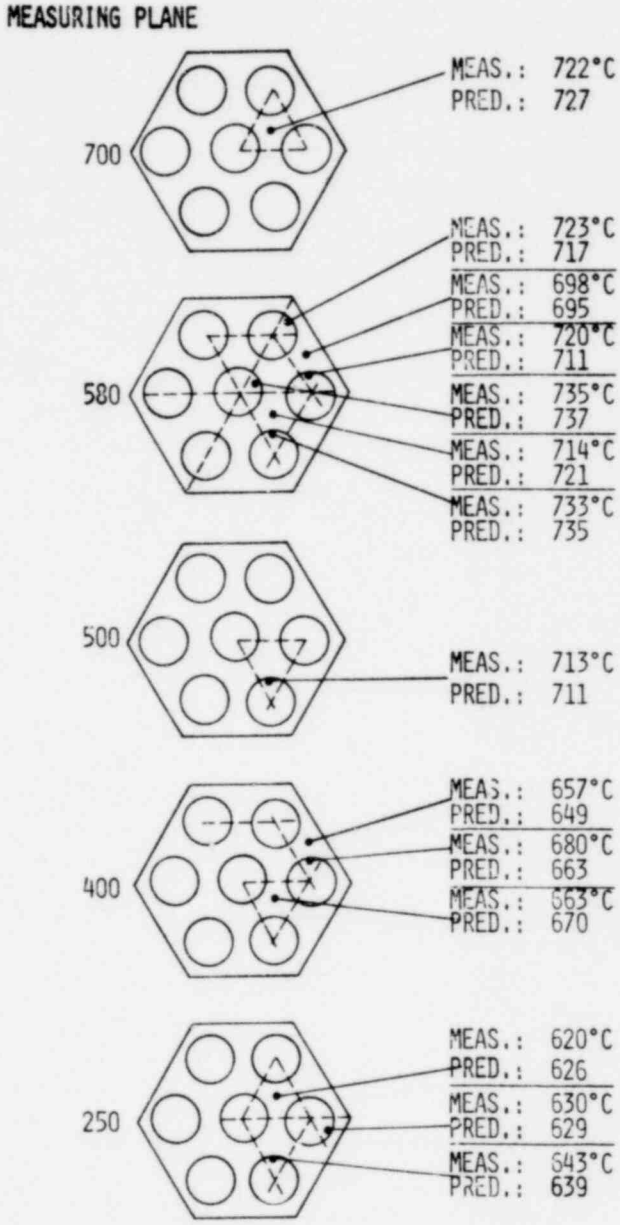

Fig. 33b.

Comparison between Measurements and Predictions. ANL Neg. No. 116-79-191R1.

REFERENCES

1. T. H. Hughes, *The Capabilities, Equations, and Solutions Procedures Used in the First Version of the FPIN Code,* Argonne National Laboratory, ANL/RAS 77-23 (July 1977).

2. Physics of Reactor Safety, Quarterly Report, January-March 1979, Argonne National Laboratory Report, ANL-79-37 (April 1979).

3. G. D. Johnson et al., *Fuel Cladding Mechanical Properties for Transient Analysis,* International Meeting on Fast Reactor Safety and Related Physics, Chicago, IL, 1976, CONF-761001, p. 998.

4. G. L. Fox, Jr., *Fuel Porosity and Crack Effects on Transient Overpower Analysis,* ASME 78-PVP-52, ASME/CSME Pressure Vessels and Piping Conference, Montreal, Canada, June 25-30, 1978.

5. Physics of Reactor Safety, Quarterly Report, July-September 1977, Argonne National Laboratory Report, ANL-77-92, pp. 4-9 (December 1977).

6. G. D. Johnson and C. W. Hunter, *Mechanical Behavior of Fast Reactor Fuel Pin Cladding Subjected to Simulated Overpower Transients,* HEDL-TME 78-13, Hanford Engineering Development Laboratory, Richland, WA (June 1978).

7. C. W. Hunter, G. D. Johnson and R. L. Fish, *Mechanical Properties During Simulated Overpower Transients of Fast Reactor Cladding Irradiated from 700-1000°F,* HEDL-TME 75-28, Hanford Engineering Development Laboratory, Richland, WA (June 1975).

8. H. M. Chung and T. F. Kassner, *Deformation Characteristics of Zircaloy Cladding in Vacuum and Steam Under Transient-Heating Conditions: Summary Report,* NUREG/CR-0344, ANL-77-31, Argonne National Laboratory (July 1978).

9. H. Yamada, *Failure of Type 316 Stainless Steel Cladding During Thermal Transients,* J. Nucl. Materials, *78,* pp. 24-32 (1978).

10. C. W. Hunter, R. L. Fish and J. J. Holmes, *Mechanical Properties of Unirradiated Fast Reactor Cladding During Simulated Overpower Transients,* Nucl. Technol., *27,* pp. 376-388 (1975).

11. O. Gotzmann and Ph. Dunner, *Fuel and Cladding Interaction, Irradiation Results: Analysis of SNR-Typical Fast Flux Experiments,* IWGFR-16, Int. Working Group on Fast Reactors Technical Committee Meeting on Fuel and Cladding Interaction, CONF-770215, Tokyo, Feb. 18-25, 1977, pp. 43-48 (1977).

12. M. Koizumi, S. Nagai, H. Furuya and T. Muto, *Review and Evaluation of Cladding Attack of LMFBR Fuel,* IWGFR-16, Int. Working Group on Fast Reactor Technical Committee Meeting on Fuel and Cladding Interaction, CONF-770215, Tokyo, Feb. 18-25, 1977, pp. 64-73 (1977).

13. Physics of Reactor Safety, Quarterly Report for October-December 1978, Argonne National Laboratory Report, ANL-79-19, pp. 17-18 (March 1979).

14. A. Padilla, Jr., *High-Temperature Thermodynamic Properties of Sodium*, HEDL-TME 77-27, Hanford Engineering Development Laboratory (February 1978).

15. F. L. Addessio, Nuclear Reactor Safety Quarterly Progress Report for the Period October 1 through December 31, 1978, Los Alamos Scientific Laboratory, p. 6 (March 1979).

16. W. H. Reed, H. B. Stewart and L. Wolf, *Applications of the THERMIT Code to 3D Thermal Hydraulic Analysis of LWR Cores*, Proc. of the Topical Meeting on Computational Methods in Nuclear Engineering, Williamsburg, VA, April 23-25, 1979, *3*, p. 9-1, Am. Nucl. Soc. (1979).

17. C. W. Stewart, C. L. Wheeler, R. J. Cena, C. A. McMonagle, J. M. Cuta and D. S. Trent, *COBRA-IV: The Model and the Method*, BNWL-2214, Pacific Northwest Laboratories, Richland, WA (July 1977).

18. V. L. Shah et al., *Some Numerical Results with the COMMIX-2 Computer Code*, NUREG-CR-0741/ANL-CT-79-30 (March 1979).

19. J. N. Lillington, *SABRE-3: A Computer Program for the Calculation of Steady State Boiling in Rod Cluster Geometry*, AEEW-M1647.

20. W. L. Chen et al., *Simple Fuel Pin Transient and Melting Model and its Application to Thermal-Hydraulics in LMFBR Subassembly*, (to be published).

21. D. S. Rowe, *COBRA-IIIC: A Digital Computer Program for Steady State and Transient Thermal Hydraulic Analysis of Rod Bundle Nuclear Fuel Elements*, BNWL-1695 (March 1973).

22. B. Greer, *A Survey of the Current State of Knowledge of Incipient Boiling Superheat in Sodium*, Argonne National Laboratory (to be published).

23. J. E. Cahalen et al., *The SAS3D LMFBR Accident Analysis Computer Code*, ANL report to be published.

24. P. A. Pizzica and P. B. Abramson, *A Numerical Model of Reactor Fuel and Coolant Motions Following Pin Failure*, Nucl. Sci. Eng., *64*, pp. 465-479 (1977).

25. M. Perks, *Revised Specification of a Reactor Model for Comparative Hypothetical Accident Studies*, WAC-D-68 (April 1975).

26. P. Royl and D. Struwe, *Specification of Relevant Parameters for Comparative TOP Whole Core Accident Simulation for the Europe Reactor*, WAC-D-77 (October 1975).

27. P. Royl and D. Struwe, *Revised Proposal for Comparative TOP Whole Core Accident Simulations*, WAC-D-82 (November 1975).

28. W. Maschek and P. Schmuck, *Additional Specifications for Comparative TOP WAC Simulation (Disassembly Phase)*, WAC-D-85 (January 1976).

29. D. H. Cho, W. L. Chen and R. W. Wright, *A Parametric Study of Pressure Generation and Sodium Slug Energy from Molten-Fuel-Coolant Interactions*, ANL-8105.

30. A. Padilla, Jr., *High-Temperature Thermodynamic Properties of Sodium*, ANL-8095 (April 1974).

31. J. F. Jackson and R. B. Nicholson, *VENUS-II: An LMFBR Disassembly Program*, ANL-7951 (September 1972).

32. Physics of Reactor Safety, Quarterly Report for October-December 1978, ANL-79-19, Argonne National Laboratory, pp. 19-28 (March 1979).

33. K. O. Reil, M. F. Young and T. R. Schmidt, *Prompt Burst Energetics Experiments: Fresh Oxide/Sodium Series*, SAND78-1561, Sandia Laboratories (1978).

34. P. L. Garner and P. B. Abramson, *Fuel and Coolant Motions Following Pin Failure: EPIC Models vs. Experiment*, Proceedings of the Specialists Workshop on Predictive Analysis of Material Dynamics in LMFBR Safety Experiments, March 13-15, 1979, Los Alamos, NM (to be published).

35. Physics of Reactor Safety, Quarterly Report for April-June 1978, ANL-78-85, Argonne National Laboratory, pp. 13-15 (1978).

36. J. Aberle et al., *Sodium Boiling Experiments in a 7-pin Bundle under Flow Rundown Conditions*, KFK-2379 (Nov. 1976).

37. L. S. Han, *Hydrodynamic Entrance Lengths for Incompressible Laminar Flow in Rectangular Ducts*, J. Applied Mechanics, *27*, p. 403 (1960).

38. H. S. Heaton, W. C. Reynolds, and W. M. Kays, *Heat Transfer in Annular Passages. Simultaneous Development of Velocity and Temperature Fields in Laminar Flow*, Int. J. Heat Mass Transfer, *7*, p. 763 (1964).

Distribution for NUREG/CR-1096 (ANL-79-76)

Internal:

J. A. Kyger
H. K. Fauske
C. E. Till
R. Avery/R. E. Henry
P. B. Abramson
I. Bornstein/L. Baker
C. Bowers
L. W. Deitrich
C. E. Dickerman
F. E. Dunn
D. Ferguson
S. H. Fistedis
P. L. Garner
E. Gelbard
H. Henryson
H. H. Hummel (2)
I. T. Hwang/W. W. Marr
Kalimullah
M. F. Kennedy
D. H. Lennox
P. Pizzica
F. G. Prohammer
B. Reynolds
D. Rose/A. J. Goldman/
J. F. Marchaterre
R. Sevy
J. J. Sienicki
W. J. Sturm
B. J. Toppel
J. B. van Erp
D. Weber
H. Wider
H. M. Domanus
J. J. Oras
B. C-J. Chen
W. T. Sha
S. K. Bhattacharyya
L. G. LeSage
D. C. Wade
P. I. Amundson/S. G. Carpenter
M. J. Lineberry
D. H. Shaftman
A. Travelli
ANL Contract File
ANL Libraries (3)
TIS Files (3)

External:

USNRC. Washington, for distribution per R7 (310)
DOE-TIC, Oak Ridge (330)
Manager, Chicago Operations and Regional Office, DOE
Chief, Office of Patent Counsel, DOE-CORO
President, Argonne Universities Association, Argonne, Ill.
Applied Physics Division Review Committee:
P. W. Dickson, Jr., Westinghouse Electric Corp., 3300 Appel Road, Bethel Park, Pa. 15102
R. L. Hellens, Combustion Engineering, Inc., Windsor, Conn. 06095
K. D. Lathrop, Los Alamos Scientific Lab., P.O. Box 1663, Los Alamos, N.M. 87545
W. B. Loewenstein, Electric Power Research Inst., P.O. Box 10412, Palo Alto, Calif. 94303
R. F. Redmond, College of Engineering, The Ohio State Univ., 2070 Neil Ave., Columbus, O. 43210
R. Sher, Dept. Mechanical Eng., Stanford U., Stanford, Calif. 94305
D. B. Wehmeyer, The Detroit Edison Co., 2000 Second Ave., Detroit, Mich. 48226
Components Technology Division Review Committee:
P. F. Cunniff, Dept. Mechanical Eng., U. Maryland, College Park, 20742
W. E. Kessler, Commonwealth Associates, Inc., 209 E. Washington Ave., Jackson, Mich. 49201
C. H. Kruger, Jr., Dept. Mechanical Eng., Stanford U., Stanford, Calif. 94305
N. J. Palladino, College of Engineering, The Pennsylvania State U., University Park, 16802
N. C. Rasmussen, Dept. Nuclear Eng., Massachusetts Inst. Technology, Cambridge, Mass. 02139
M. A. Schultz, Dept. Nuclear Eng., The Pennsylvania State U., University Park, 16802
A. Sesonske, Dept. Nuclear Eng., Purdue U., West Lafayette, Ind. 47906
H. Thielsch, ITT Grinnell Corp., 260 W. Exchange St., Providence, R.I. 02901
Y. C. L. S. Wu, Energy Conversion Div., U. Tennessee Space Inst., Tullahoma, 37388
C. Erdman, U. Virginia, Charlottesville, Va. 22904
K. O. Ott, Purdue U., West Lafayette, Ind. 47906
R. Lancet, Atomics International, P.O. Box 309, Canoga Park, Calif. 91304